ARL-TR-10062 ● Feb 2025

Development of Diamond-Based Materials Systems for High-Power RF Electronics: Fourth-Year Report

by Pulickel M Ajayan, Robert Vajtai, Xiang Zhang, Anand B Puthirath, Abhijit Biswas, Eliezer Oliveira, Chenxi Li, Harikishan Kannan, Tia Gray, Jacob Elkins, Tim Pieshkov, Jishnu Murukeshan, Tony Ivanov, Nicholas R Jankowski, A Glen Birdwell, Mahesh Neupane, Bradford B Pate, Elias Garratt, Sergey Rudin, Dmitry Ruzmetov, Pankaj Shah, James Weil, Leonard De La Cruz, Derwin Washington, Stephen B Kelley, and Brittany Kaufmann

NOTICES

Disclaimers

The findings in this report are not to be construed as an official Department of the Army position unless so designated by other authorized documents.

Citation of manufacturer's or trade names does not constitute an official endorsement or approval of the use thereof.

Destroy this report when it is no longer needed. Do not return it to the originator.

ARL-TR-10062 ● FEB 2025

Development of Diamond-Based Materials Systems for High-Power RF Electronics: Fourth-Year Report

Pulickel M Ajayan, Robert Vajtai, Xiang Zhang, Anand B Puthirath, Abhijit Biswas, Eliezer Oliveira, Chenxi Li, Harikishan Kannan, Tia Gray, Jacob Elkins, Tim Pieshkov, and Jishnu Murukeshan
Rice University

Tony Ivanov, Nicholas R Jankowski, A Glen Birdwell, Mahesh Neupane, Elias Garratt, Sergey Rudin, Dmitry Ruzmetov, Pankaj Shah, James Weil, Leonard De La Cruz, and Derwin Washington
DEVCOM Army Research Laboratory

Bradford B Pate
US Naval Research Laboratory

Stephen B Kelley and Brittany Kaufmann
General Technical Services

REPORT DOCUMENTATION PAGE

1. REPORT DATE	2. REPORT TYPE	3. DATES COVERED	
		START DATE	END DATE
February 2025	Technical Report	5/01/2023	4/30/2024

4. TITLE AND SUBTITLE
Development of Diamond-Based Materials Systems for High-Power RF Electronics: Fourth-Year Report

5a. CONTRACT NUMBER	5b. GRANT NUMBER	5c. PROGRAM ELEMENT NUMBER

5d. PROJECT NUMBER	5e. TASK NUMBER	5f. WORK UNIT NUMBER
W911NF1920269		

6. AUTHOR(S)
Pulickel M Ajayan, Robert Vajtai, Xiang Zhang, Anand B Puthirath, Abhijit Biswas, Eliezer Oliveira, Chenxi Li, Harikishan Kannan, Tia Gray, Jacob Elkins, Tim Pieshkov, Jishnu Murukeshan, Tony Ivanov, Nicholas R Jankowski, A Glen Birdwell, Mahesh Neupane, Bradford B Pate, Elias Garratt, Sergey Rudin, Dmitry Ruzmetov, Pankaj Shah, James Weil, Leonard De La Cruz, Derwin Washington, Stephen B Kelley, and Brittany Kaufmann

7. PERFORMING ORGANIZATION NAME(S) AND ADDRESS(ES)	8. PERFORMING ORGANIZATION REPORT NUMBER
DEVCOM Army Research Laboratory ATTN: FCDD-RLA-LF 2800 Powder Mill Road Adelphi, MD 20783	ARL-TR-10062

9. SPONSORING/MONITORING AGENCY NAME(S) AND ADDRESS(ES)	10. SPONSOR/MONITOR'S ACRONYM(S)	11. SPONSOR/MONITOR'S REPORT NUMBER(S)

12. DISTRIBUTION/AVAILABILITY STATEMENT
DISTRIBUTION STATEMENT A. Approved for public release: distribution unlimited.

13. SUPPLEMENTARY NOTES
ORCIDs: Tony Ivanov, 0000-0002-1472-788X; Nicholas R Jankowski, 0000-00018648-3055; A Glen Birdwell, 0000-0001-5235-3260; Mahesh Neupane, 0000-0002-4806-6581; Elias Garratt, 0000-0002-0331-3876; Dmitry Ruzmetov, 0000-0002-0688-1908; Pankaj Shah, 0000-0003-2356-5664; James Weil, 0000-0001-8125-4587

14. ABSTRACT
This report details the fourth-year research effort that is part of the cooperative agreement between Rice University and the DEVCOM Army Research Laboratory (ARL). The project aims to develop diamond and diamond-based heterostructures for the next-generation of ultra-wide bandgap electronic devices, with performances far exceeding those of wide bandgap materials-based devices. The Rice University team is primarily focused on cultivating high-quality single-crystal diamond (SCD) substrates and heterostructures, involving diamond and boron nitride (BN). Simultaneously, ARL is constructing high-performance electronic devices based on diamond. Rice has established a world-class facility dedicated to growing SCDs and heterostructures. The work in the first, second, and third years encompassed activities such as BN growth and transfer on commercially available diamond substrates, ion implantation for doping, BN structure deposition on diamond, development of unique metrology tools for characterizing diamond surfaces and heterostructures, surface modification through hydrogenation and oxygenation, theoretical modeling to comprehend growth, and surface characteristics of diamond and diamond/BN heterostructures. In the fourth year, attempts were made to grow single-crystal diamond wafers, and growth protocols were optimized for various thicknesses of epilayers and growth rates on desired substrates. For BN nitride growth, there is an ongoing exploration of the phase diagram for different BN phases (hexagonal, cubic, turbo-static, wurtzite). Improvements in metrology aspects, enhancing resolution in microscopy and spectroscopy and THz spectroscopy for grown single-crystal structures and epitaxially grown heterostructures, are optimized. Surface functionalization approaches are being employed to enhance the functionalities of diamond surfaces, and these are being comprehended through theoretical and computational modeling. Also, reactive ion etching is being employed for clean and low-roughness diamond wafers. Additionally, experiments involving low-energy ion implantation are being conducted to n-dope diamond wafers and produce color centers. The synergy between the two institutions fosters a close working relationship, leading to the synthesis of controlled diamond materials and their use in high-power devices.

15. SUBJECT TERMS
diamond, hexagonal/cubic boron nitride, interface characterization, surface modification, DFT/MD simulations, adhesion energy, low-energy ion implantation, n-type diamond, Electromagnetic Spectrum Sciences

16. SECURITY CLASSIFICATION OF:			17. LIMITATION OF ABSTRACT	18. NUMBER OF PAGES
a. REPORT	b. ABSTRACT	C. THIS PAGE		
UNCLASSIFIED	UNCLASSIFIED	UNCLASSIFIED	UU	77

19a. NAME OF RESPONSIBLE PERSON	19b. PHONE NUMBER *(Include area code)*
A Glen Birdwell	(301) 394-0601

STANDARD FORM 298 (REV. 5/2020)
Prescribed by ANSI Std. Z39.18

Contents

List of Figures

List of Tables

1. Introduction

With the increasing demand for silicon (Si) electronics in terms of power and energy considerations, wide bandgap semiconductors have become a viable option, enabling new device architectures and the use of new semiconductor materials.[1] Among these, silicon carbide (SiC) and gallium nitride (GaN)-based devices have been explored widely.[2–4] However, it has been realized recently that diamond, an ultra-wide bandgap (UWBG) (>5 eV) material, has significant advantages compared to GaN or SiC if implemented in high power devices.[5] Owing to the ultra-high bandgap and extremely high thermal conductivity, diamond has been touted as the next-generation material for high voltage, high power, high temperature, and high-frequency devices.[6] Despite these advantages, bulk diamond, as an insulating material, requires surface terminations such as hydrogen (H) and oxygen (O) to achieve conductive characteristics. In particular, the band structure in H-terminated diamond with negative electron affinity (NEA) allows it to act as easy electron emitters to vacuum levels, at higher voltages, which can be captured in a dielectric layer placed on top of the diamond, and in the process also generating high hole conduction in the diamond layer.[7] Hence, diamond—with the right kind of interface dielectric layer and doping—can become an exciting building block for transistors, the drivers of the semiconductor industry. The high thermal conductivity[8] of diamond also allows excellent intrinsic thermal management, a bottleneck with the existing Si-based semiconductor device technologies.

The advantages aside, there are significant challenges in realizing diamond-based device technologies. These are mainly related to the growth of high-quality diamond films, selection and adoption of the right interface dielectric layer, controlled doping to enable device polarity, and contact issues with metal lines. In recent years, various attempts have been made to address these issues and improve the performance of diamond devices. Recent advances in chemical vapor deposition (CVD)[9] of diamond have resulted in the ability to grow good quality single- and polycrystalline films over areas ranging from a few millimeters to several centimeters.[10] For the dielectric layer over diamond, several metal-oxide films have been explored (alumina, molybdenum trioxide, etc.) with varying degrees of success based on the interface structure and epitaxy and interfacial charges. For the doping part, various approaches have enabled p-type and n-type structures with dopants such as boron (B) and phosphorus (P).[11] However, uniform and controlled doping has been extremely challenging leading to techniques that alter diamond surface terminations (H or O). These surface modifications alter the bandgap and electronic structure of diamond and enable higher charge carrier densities and mobilities.

Specific project objectives are as follows:

- Establishing a CVD facility for the growth of large-area, high-quality diamond films, vapor phase doping methods, and electronic and thermal characterization tools for the grown diamond films and diamond-based heterostructures.
- Developing and optimizing various approaches that enable the synthesis of heteroepitaxial diamond/boron nitride (BN) heterostructures, including diamond/BN (hexagonal and cubic), diamond/h-boron carbon nitride (BCN), and other multilayer structures including the gate dielectric.
- Developing methods that would enable various types of doping of the diamond films to engineer its bandgap and electronic structure and understanding the interface electronic properties of doped diamond films and BN layers.
- Engineering low resistance contacts between diamond/BN/dielectric films and selection of metals and alloys and integration and testing these in field-effect transistor diamond devices.
- Developing close collaboration with the US Army Combat Capabilities Development Command Army Research Laboratory to develop device architectures for the diamond-BN heterostructures grown at Rice University and fabricating and testing these devices both at Rice and DEVCOM Army Research Laboratory. The goal will be to achieve far better device performance compared to existing diamond wide bandgap devices, based on well-defined device metrics.
- Explore, in subsequent years, novel applications, outside of semiconductor device applications, for the diamond-BN heterostructures such as quantum sensing, single-photon emission, thermal management, and optoelectronics.

2. Events

Table 1 lists significant meetings and laboratory visits.

Table 1 Events

Events	Date	Location
Biweekly meeting	2023/01/11 to present	Online
Danish space delegation's visit	2023/2/2	Rice University
Tim Pieshkov's visit to Oak Ridge National Laboratory (ORNL)	2023/5/12–7/12	ORNL; Oak Ridge, Tennessee
Tia Gray's internship at ARL	2023/5/12–8/12	ARL; Adelphi, Maryland
New Diamond and Nano Carbons (NDNC) conference 2023	2023/6/18–6/22	East Lansing, Michigan
U.S. Senate staff member's visit	2023/8/8	Rice University
Dr. David Stepp (Army Research Office [ARO]) and ARO/ARL staff's visit	2023/10/4–10/5	Rice University
Dr. Brett A. Seidle's (U.S. Navy) visit	2023/10/13	Rice University
Dr. Michael Bakas' (ARL South Director) visit	2023/12/12	Rice University
The annual review meeting	2024/2/6	Rice University
Anand Puthirath's visit to Helmholtz-Zentrum Dresden-Rossendorf (HZDR), Germany	2022/9/22	Dresden, Germany
Anand Puthirath's visit to Johannes Gutenberg University (JGU) of Mainz	2023/06/01	Mainz, Germany

3. Materials of Interest and Growth Approaches

3.1 Growth of Smooth Diamond Epilayer

The surface smoothness of epitaxial diamond films plays a pivotal role in various prospective applications such as electronic devices, quantum sensors, and optical windows. The diamond polishing process, while demanding considerable effort due to the extreme hardness of diamond, unavoidably introduces surface defects and subsurface damage. Consequently, achieving a smooth diamond epilayer without the necessity for polishing becomes significantly crucial. However, it has been demonstrated that preparing an atomically smooth diamond is immensely challenging. First, hillocks and nonepitaxial crystallites, which make the surface rough, need to be eliminated during the growth. Second, the growth conditions and substrate orientation require elaborate optimization to achieve step-flow or lateral growth. As a result, limited reports in literature have achieved this.

Figure 1 illustrates the characterization of commercial diamond substrates, including Element Six standard-grade CVD-grown diamond (referred to as CVD substrate) and Element Six high-pressure, high-temperature (HPHT) diamond (referred to as HPHT substrate) following super-polishing by Applied Diamond. All substrates underwent acid cleaning using HCl/HNO_3 and H_2SO_4/HNO mixtures. Despite the low surface roughness of the CVD-grown diamond substrate, a high density of pits and polishing lines can be observed in atomic force microscopy (AFM) images in Fig. 1a and 1b. The Raman spectra in Fig. 1c shows the presence of nitrogen-related peaks. In contrast, the HPHT diamond substrate displays an exceptionally smooth surface with surface roughness of 0.6 nm (Fig. 1e and 1f) and a distinct diamond Raman peak (Fig. 1g). X-ray diffraction (XRD) rocking curve measurements in Fig. 1d and 1h reveal the full width at half maximum (FWHM) of (400) peak is 30.82 inches for CVD substrate and 30.46 inches for HPHT substrate, respectively.

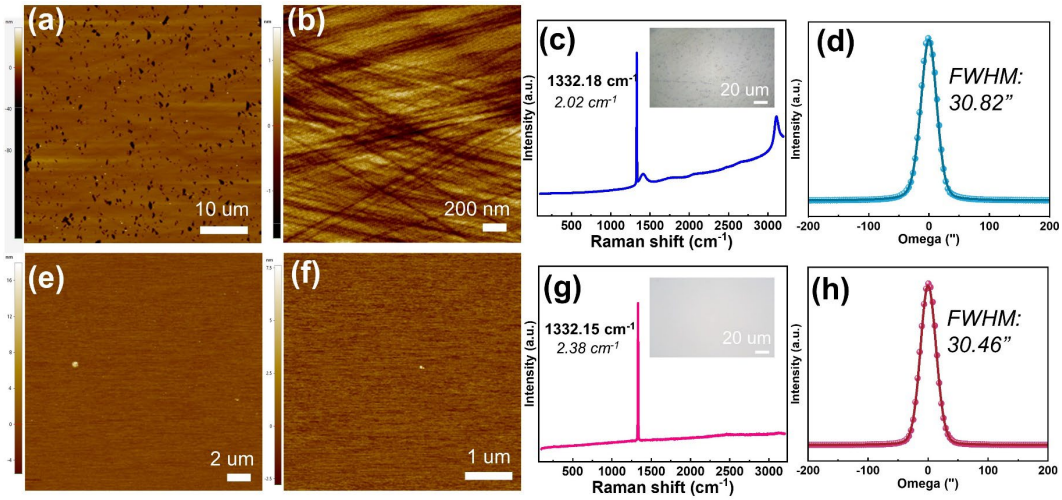

Fig. 1 (a,b) AFM images, (c) Raman spectra, and (d) XRD (400) rocking curve of CVD substrate. (e,f) AFM images, (g) Raman spectra, and (h) XRD (400) rocking curve of HPHT substrate.

Subsequently, H_2 plasma etching was performed on the substrates to eliminate the subsurface defects. Following the etching process, additional peaks emerged in the Raman spectra of CVD substrate (Fig. 2a). These peaks are potentially associated with defects and dislocations. A higher density of pits was found on the surface in both optical (Fig. 2b) and AFM images (Fig. 2c–2e). In contrast to the randomly distributed pits on the original surface, the etch pits exhibited uniform rectangular shapes and alignment with the surface terrace. These pits are thought to originate from dislocations within the bulk diamond substrate. Conversely, the Raman spectra of HPHT substrate post etching remained like the original spectra (Fig. 2f). Nearly no etch pits can be found in optical image (Fig. 2g) or AFM images (Fig. 2h and 2i), indicating a low dislocation density in HPHT substrate. The surface roughness was reduced to 0.3 nm after the etching process.

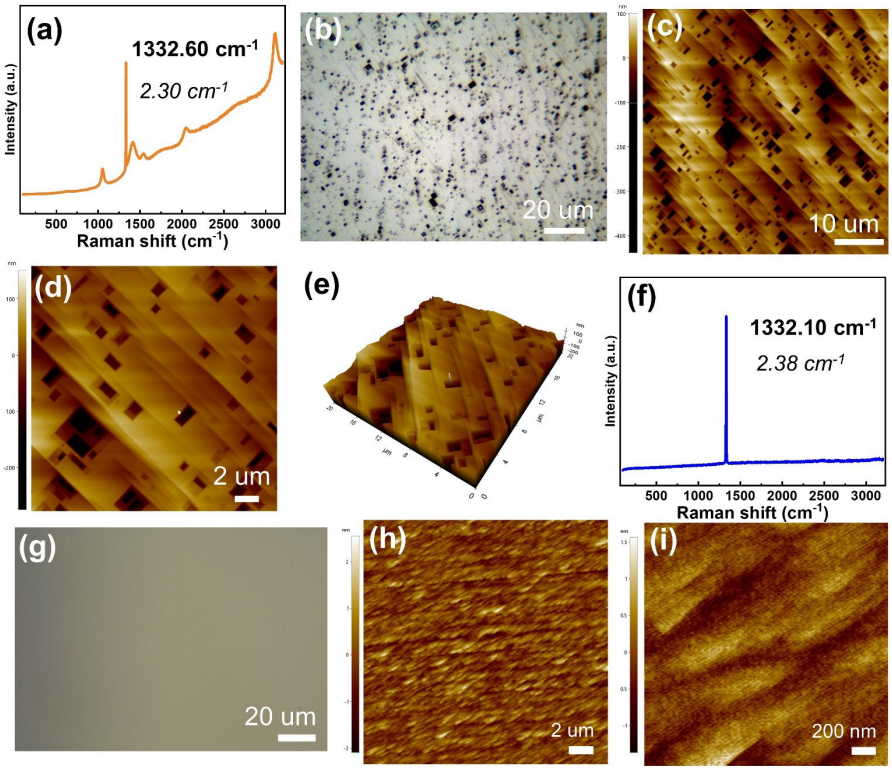

Fig. 2 (a) Raman spectra, (b) optical image, (c,d) AFM height image, and (e) 3D image of CVD substrate. (f) Raman spectra, (g) optical image, (h,i) AFM height image of HPHT substrate.

After the H_2 plasma etching, epilayer growth was carried out using 1% CH_4/H_2. To investigate the surface morphology evolution, four sequential epilayer growths were performed on the CVD substrate, each of which lasted 2–3 h. Following the first growth, both the optical image and AFM image in Fig. 3a show a significant reduction in the number of pits, accompanied by a decrease in their lateral dimensions. After the second growth, etch pits were scarcely observable in both the optical image and AFM image (Fig. 3b), indicating that they have been mostly filled through the growth process. After the third and fourth growths, the diamond surface exhibited exceptional smoothness without any pits or hillocks (Fig. 3c and 3d). The surface roughness of the epilayer after the four growths was measured to be 0.9 nm in Fig. 3e. Simultaneously, the Raman spectra in Fig. 3f illustrates the disappearance of defect-related peaks after growth, while the intensity of diamond peak increased with growth. The low FWHM of XRD (100) rocking curve in Fig. 3g and (111) rocking curve in Fig. 3h indicate the high crystallinity of the epilayer. These outcomes underscore that the epitaxially grown films not only render the surface smooth but also manifest higher quality and purity compared to the CVD substrate.

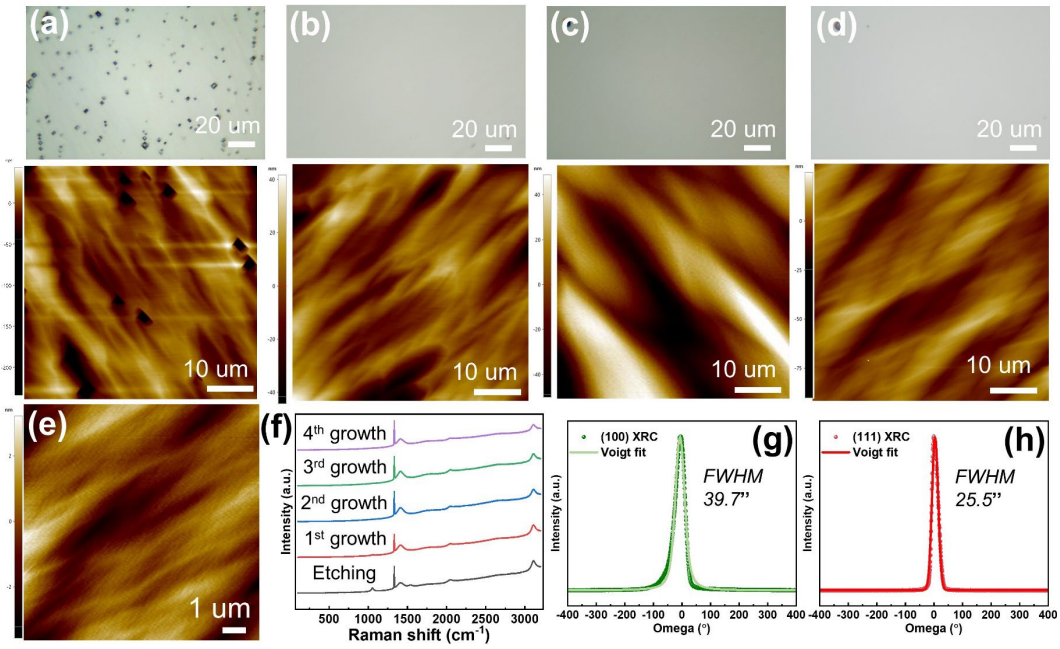

Fig. 3 (a–d) Optical image and AFM image of epilayer surface after each growth process. (e) High-resolution AFM image of epilayer surface after four growths. (f) Raman spectra evolution of epilayer after etching and growth. (g) XRD (100) rocking curve and (h) XRD (111) rocking curve.

On the HPHT substrate, one growth process resulted in an approximately 0.9-um-thick epilayer. Remarkably, the AFM images in Fig. 4a and 4b depict an exceptionally low surface roughness of the epilayer—only 0.3 nm. The Raman spectra presented in Fig. 4c shows a sharp diamond peak like that of the original substrate. Optical imaging of the entire surface in Fig. 4d reveals the absence of nearly any hillocks. Laser microscopy (Fig. 4e) further confirmed that the surface roughness is less than 0.7 nm, surpassing the instrument resolution. The X-ray photoelectron spectroscopy (XPS) survey scan in Fig. 4f reveals the surface primarily consists of carbon (C) with a small content of oxygen. No other contaminants were detected. XRD rocking curve measurements of (400) (113) (111) peaks were presented in Fig. 4g–4i, respectively. Their remarkably low FWHM reflects the high crystallinity of the epilayer. These findings indicate a high-quality epilayer with an ultra-smooth surface has been prepared on the HPHT substrate.

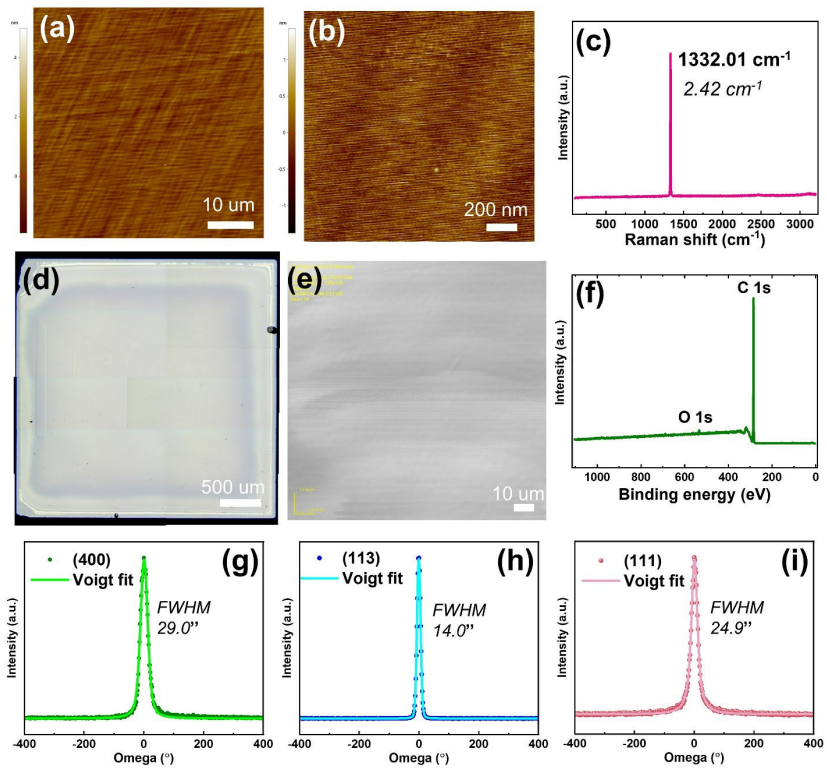

Fig. 4 (a,b) AFM images, (c) Raman spectra, (d) optical image, (e) laser microscope image, and (f) XPS survey spectra of epilayer grown on HPHT substrate. XRD rocking curve measurements of (g) (400), (h) (113), and (i) (111) peaks.

3.2 Ion Implantation and Lift-Off Process

Due to its highest hardness and exceptional mechanical properties, manufacturing diamond wafers through slicing or polishing is much more challenging compared to other materials. While laser cutting has proven effective for slicing diamond crystals, note that the kerf loss is directly related to the cutting depth. Moreover, after lasing cutting, further polishing is necessary to achieve a smooth surface before subsequent manufacturing steps. The most efficient method for producing diamond wafers without traditional cutting involves the ion implantation and lift-off process. In the process, high-energy ion implantation is initially performed on the diamond substrates, with carbon and oxygen ions being the most used ion species. For example, when the carbon ion implantation energy is set at 3 MeV and the ion dose is 2×10^{16} ion/cm^2, an amorphous carbon (a-C) layer is expected to form at approximately 1.6 um beneath the surface while leaving a minimally damaged layer near the surface. Subsequently, an epilayer growth is carried out on the substrate, during which the high temperature can transform the a-C layer into a graphite layer. Next, the graphite layer is removed via electrochemical etching, allowing the CVD-grown epilayer to be separated from the substrate. The surface of the separated substrate remains smooth and exhibits a morphology like the

original substrate, which can be reused repeatedly for growth or device fabrication without the need for polishing.

In this study, the high energy (3 MeV) ion implantation was carried out on Element Six standard-grade CVD-grown diamond at a dose of 2×10^{16} ion/cm^2. After ion implantation, it can be seen from Fig. 5a that the diamond substrate becomes nontransparent. Raman spectra in Fig. 5b show a broadening and weakening of the diamond peak, accompanied by the emergence of graphite peaks. The AFM images in Fig. 5c and 5b and optical image in Fig. 5e demonstrate the surface morphology and roughness remain comparable to the original surface. In the XRD 2 theta/omega scan in Fig. 5f, new peaks appear around 115°~118°, possibly attributed to damage induced by the ion implantation. However, the rocking curve measurement of the (400) peak remains similar.

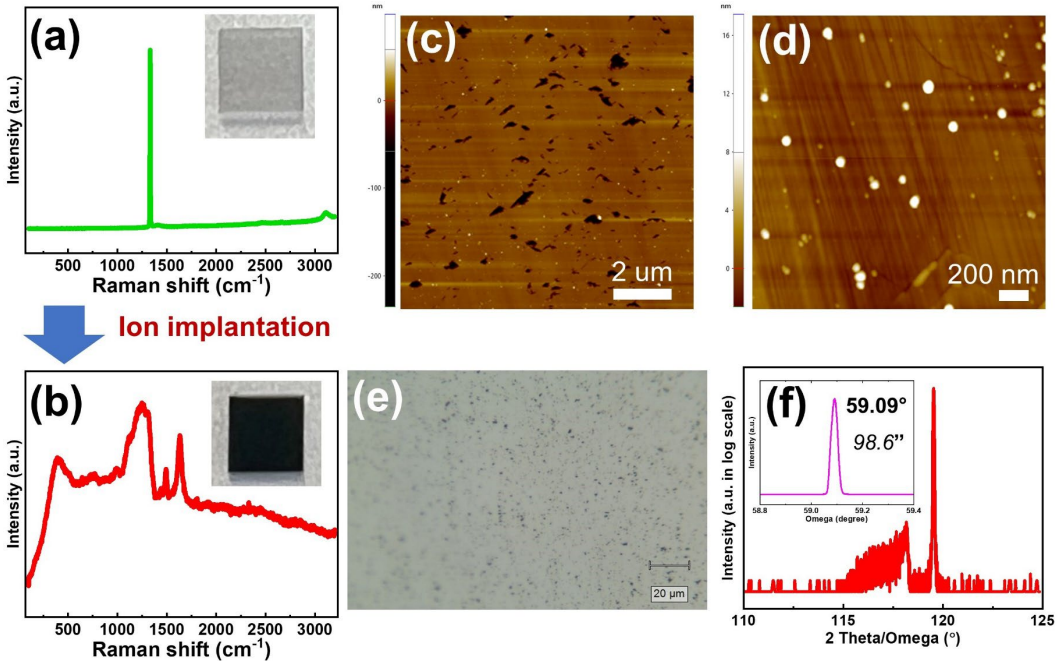

Fig. 5 Raman spectra and photograph of diamond substrate (a) before and (b) after ion implantation. (c,d) AFM images, (e) optical image, and (f) XRD measurements of implanted diamond substrate.

Epilayer growth was performed on three implanted substrates. For the first implanted substrate, 4% CH_4/H_2 was utilized for the growth, resulting in the observation of high hillocks and nonepitaxial crystallites in the optical image shown in Fig. 6a. Raman spectra in Fig. 6b demonstrate the restoration of an intense diamond peak. As displayed in the XRD 2 theta/omega scan (Fig. 6c), the damage-related peak disappeared, while the width of (400) peak slightly increases. The FWHM of (400) rocking curve peak in Fig. 6d decreases, indicating improved crystallinity of the epilayer compared to the substrate. On the second implanted

substrate, four growths using 1% CH_4/H_2 and three growths using 2% CH_4/H_2 were conducted sequentially. The optical image in Fig. 6e reveals a reduction in hillock density compared to the first sample. Notably, the surface among the hillocks appears very smooth, as shown in the optical image (Fig. 6f) and AFM image (Fig. 6g), with a measured surface roughness of 0.2 nm. Figure 6h illustrates the evolution of Raman spectra on the epilayer after each growth. It can be observed that the intensity of diamond peak continues increasing with growth, while other peaks and overall background were reduced. For the third implanted substrate, two epilayer growths were carried out using 1% CH_4/H_2, followed by another growth using 4% CH_4/H_2 and 0.4% O_2/H_2. Figure 7i shows a significant reduction in both the dimensions and density of hillocks. The surface roughness of the smooth area (Fig. 6j) was measured to be 0.7 nm by AFM (Fig. 6k). The Raman spectra in Fig. 6i illustrates the first two slow growths lead to a small increase of diamond peak intensity, while the final fast growth significantly enhances the diamond peak intensity.

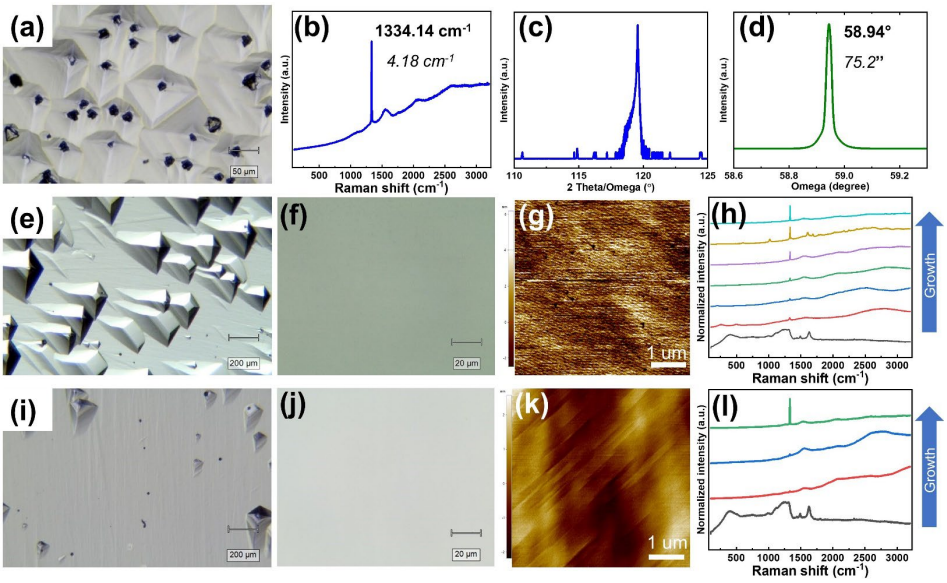

Fig. 6 (a) Optical image, (b) Raman spectra, (c) XRD 2 theta/omega measurement, and (d) (400) rocking curve measurement of first implanted sample. (e,f) Optical image, (g) AFM image, and (h) Raman spectra evolution on the second implanted sample. (i,j) Optical images, (k) AFM image, and (l) Raman spectra evolution on the third implanted sample.

After epilayer growth, the scanning electron microscopy (SEM) image in Fig. 7a taken from the side view reveals that the edges of the sample have been covered. To expose the graphite layer, it becomes necessary to remove these coverings. Hence, a wafer polisher with diamond lapping film was employed to grind the edges. The SEM image (Fig. 7b) and optical image (Fig. 7c) demonstrate the edges after polishing, with the graphite layer clearly visible. Above the graphite layer, there are epilayer and low-damaged substrate layer. The width of the low damaged

substrate layer measures approximately 1.5 um, aligning with the theoretical result. Next, Raman measurements were performed on the edge. The Raman spectra collected from the epilayer region in Fig. 7d exhibit a sharp diamond peak without any other peak or background (Fig. 7e). In contrast, the Raman spectra collected from the substrate region show intensive nitrogen-related peaks (Fig. 7f). Raman mapping using the intensity of nitrogen-related peak at 1416 cm^{-1} (Fig. 7g) confirms that nitrogen is predominantly found in the substrate region, including the low damaged substrate region. Figure 7h shows the Raman mapping using the intensity of diamond peak at 1332 cm^{-1}. Both the epilayer and the substrate exhibit high intensities, while the low damaged substrate region shows weak signals, indicating low crystallinity. Figure 7i presents Raman mapping using the intensity ratio of diamond peak at 1332 cm^{-1} to nitrogen related peak 1416 cm^{-1}. It can be observed that the high-tensity region corresponds well with the epilayer region. All these experimental results not only align with theoretical expectations but also confirm a significant improvement in the quality and purity of the epilayer compared to the substrate.

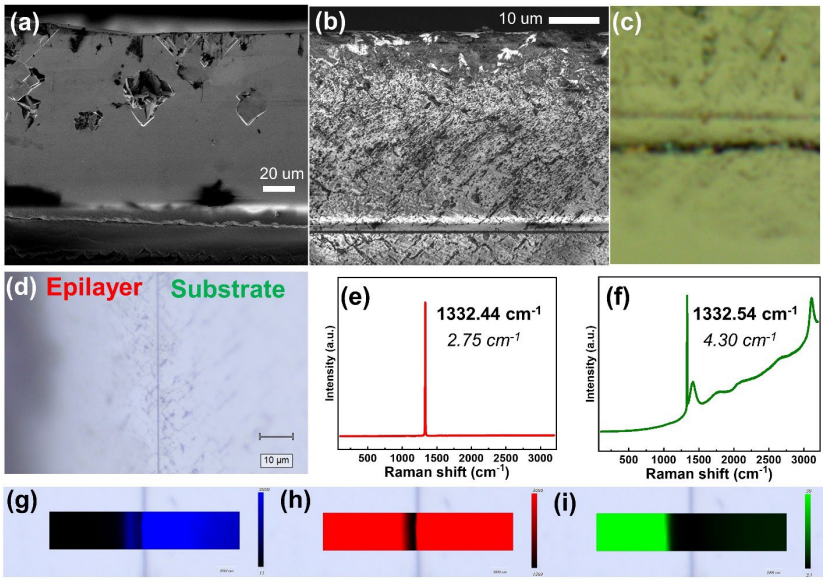

Fig. 7 (a) SEM image of an edge after growth. (b) SEM image and (c) optical image of edges after polishing. (d) Optical image showing the graphite layer in the middle. Raman spectra collected from (e) epilayer region and (f) substrate region. Raman mapping using the intensity of the peak at (g) 1416 cm^{-1}, (h) 1332 cm^{-1} and (i) the peak intensity ratio of these two.

By employing electrochemical etching on the graphite layer in the K_2SO_4/H_2SO_4 electrolyte, the epilayer was effectively detached from the substrate, as evidenced in Fig. 8a. Only a small piece of the epilayer remained attached. Raman spectra collected from both the substrate and lifted layer show intensive diamond peak in Fig. 8b and 8c, respectively. The optical image (Fig. 8d) and AFM images (Fig. 8e and 8f) of the substrate after the lift-off show a morphology similar to the original surface. These results suggest the surface can be reused for future growth.

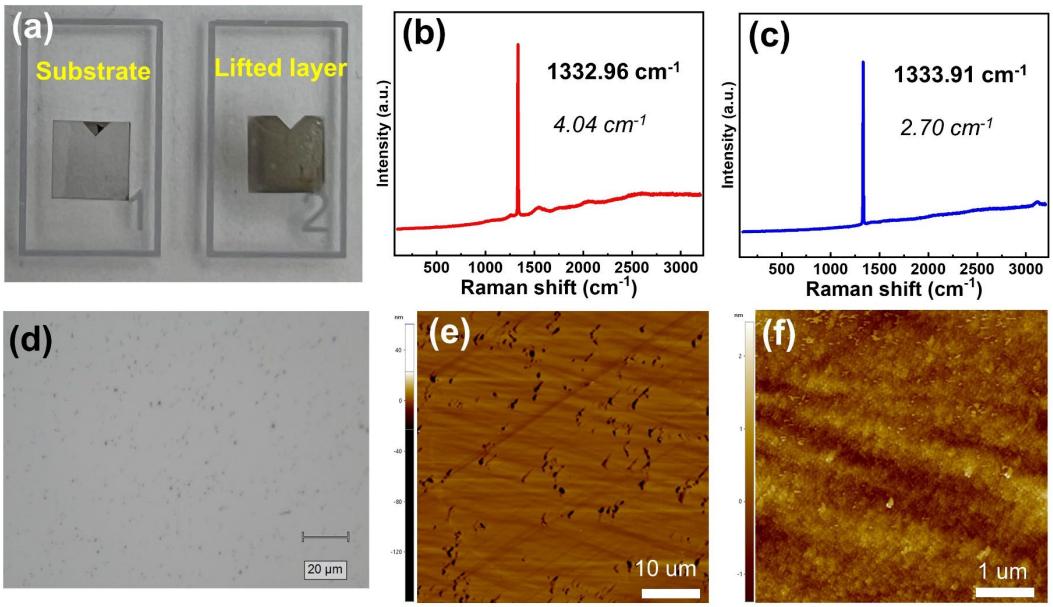

Fig. 8 (a) Photograph of substrate and lifted layer. Raman spectra of (b) lifted layer and (c) substrate. (d) Optical image and (e,f) AFM images of the substrate surface.

4. Epitaxial c-BN Phase Thin Film Growth on Single-Crystal Diamond

4.1 Introduction

UWBG semiconductors are central to the advancement of next-generation high-power radio frequency (RF) electronics, thanks to their exceptional chemical, thermal, and mechanical stability. As indicated by the Baliga figure of merit (BFOM) for power loss (Fig. 9a), UWBG diamond and cubic BN (c-BN)—the two strongest materials—exhibit significant promise for devices requiring very high breakdown voltage (~1000 V) and low power loss, making them well-suited for RF and power electronics. Diamond and c-BN are structurally, chemically, thermally, optically, and electrically compatible with each other, with c-BN presenting itself as a formidable competitor to diamond as a superhard engineering material. The primary distinction lies in the doping capabilities: while c-BN can be doped with both p- and n-type dopants, diamond can only be p-type doped. Consequently, an optimal high-mobility transistor could be realized by establishing an electronic-quality interface between n-type c-BN and p-type diamond, facilitating the creation of field-effect transistor (FET) devices with exceptionally high mobility (Fig. 9b).

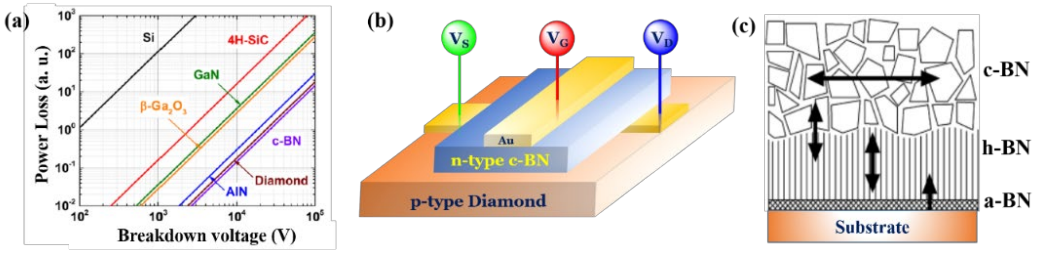

Fig. 9 (a) UWBG semiconductors with BFOM. (b) FET with c-BN and diamond. (c) Growth of various phases of BN.

Nevertheless, achieving the growth of electronic-quality (i.e., single-crystalline, defect-free, and ultra-smooth) pure and doped (001) c-BN thin films on (001) diamond substrates remain the "Holy Grail" for materials scientist and device engineers. The growth of electronic-quality c-BN thin films remains challenging, primarily due to the intricate pressure–temperature phase diagram of B and N, which results in the formation of mixed-phase films on diamond surfaces. Depending on pressure and temperature conditions, BN can manifest various phases (e.g., h-BN, c-BN, r-BN, and w-BN) (Fig. 9c). Our objective for device fabrication is to cultivate metastable epitaxial c-BN thin films on (001) single-crystal diamond (SCD) substrates, ensuring smooth interfaces.

4.2 Investigation of Bulk c-BN Phase Stability and Phase Diagram

The phase stability of c-BN is an important aspect in materials science and semiconductor industry. As a crystalline form of BN, c-BN has diamond-like structure. It is often referred to as the second hardest material after diamond. The stability of the cubic phase of BN depends on various factors such as pressure and temperature. Under ambient conditions, hexagonal BN (h-BN) is the stable form, but at HPHT, it can transform into the cubic phase. Research indicates that c-BN is metastable at atmospheric pressure and room temperature (RT), but it becomes stable under high-pressure conditions. The high-pressure phase stability of c-BN is significant in applications such as superhard materials, abrasives, and as an analog to diamond in various semiconductor electronics. Researchers continue to explore the properties and potential applications of c-BN under extreme conditions.

First to grow the cubic BN films, our approach was to make a polycrystalline c-BN as a target material for the laser ablation. However, the single-crystal cubic BN or even good quality polycrystalline c-BN powder were not available in the market. Fortunately, MSE Supplies LLC (Tucson, Arizona) provided cubic BN on two different grain sizes (2–3 and 30–40 um). Thus, we first characterized the c-BN and h-BN powders to identify the characteristic features of respective phases, which

should further help to distinguish the nature of grown BN phases on diamond. By using extensive characterizations (XRD, XPS, Raman, Fourier transform infrared [FTIR], and SEM), images show different characteristic features for 2D h-BN and 3D c-BN. From XRD, h-BN shows (002) peak, whereas, for c-BN (111) is the most energetic phase (Fig. 10). In XPS, both h-BN and c-BN show B-N bonding peak for B1s and N1s core; however, distinguishably, h-BN shows additional pi-plasmon peak, which is absent for the c-BN. Field emission scanning electron microscopy (FESEM) images clearly show the sheet-like and 3D particles for h-BN and c-BN. In Raman and FTIR spectroscopy E_{2g} Raman modes at 1365 cm^{-1} for h-BN, whereas transverse optical (TO) and longitudinal optical (LO) modes at 1054 and 1304 cm^{-1} are formed for c-BN.

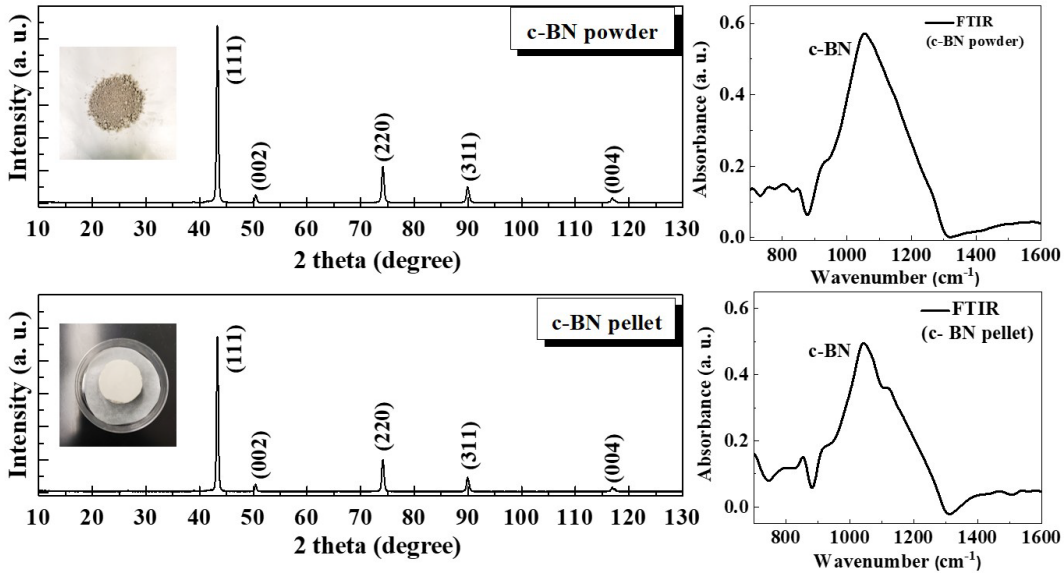

Fig. 10 Characterization of c-BN powder and a pressed pellet to be used for the laser ablation

At first, we tried to make the pristine c-BN phase target materials (1-inch-diameter disk) for the laser ablation, as pulsed laser deposition (PLD) is a single target ablation process (Fig. 10). So, we grounded the few grams of c-BN powder and pressed it and sintered the disk at 1000 °C for 12 h in vacuum. After sintering it formed a pellet, but was not so dense, and the density of the disk was below 1 g/cm^3 (the actual theoretical density of c-BN is 3.48 g/cm^3). We tried to use the disk for the laser ablation; however, it was not adequate for the growth as it was not a dense solid (Fig. 11). We also obtained the c-BN powder with particle size of 30–40 um and performed the similar characterizations (as in Raman spectra it shows several extra shoulder peaks along with the high LO and TO modes), which shows more defective nature of c-BN as producing c-BN with good quality is a challenge due to its metastable nature. We tried to make the c-BN pellet with this powder material as well; however, it shows the similar trend on not forming a compact disk (Fig. 11).

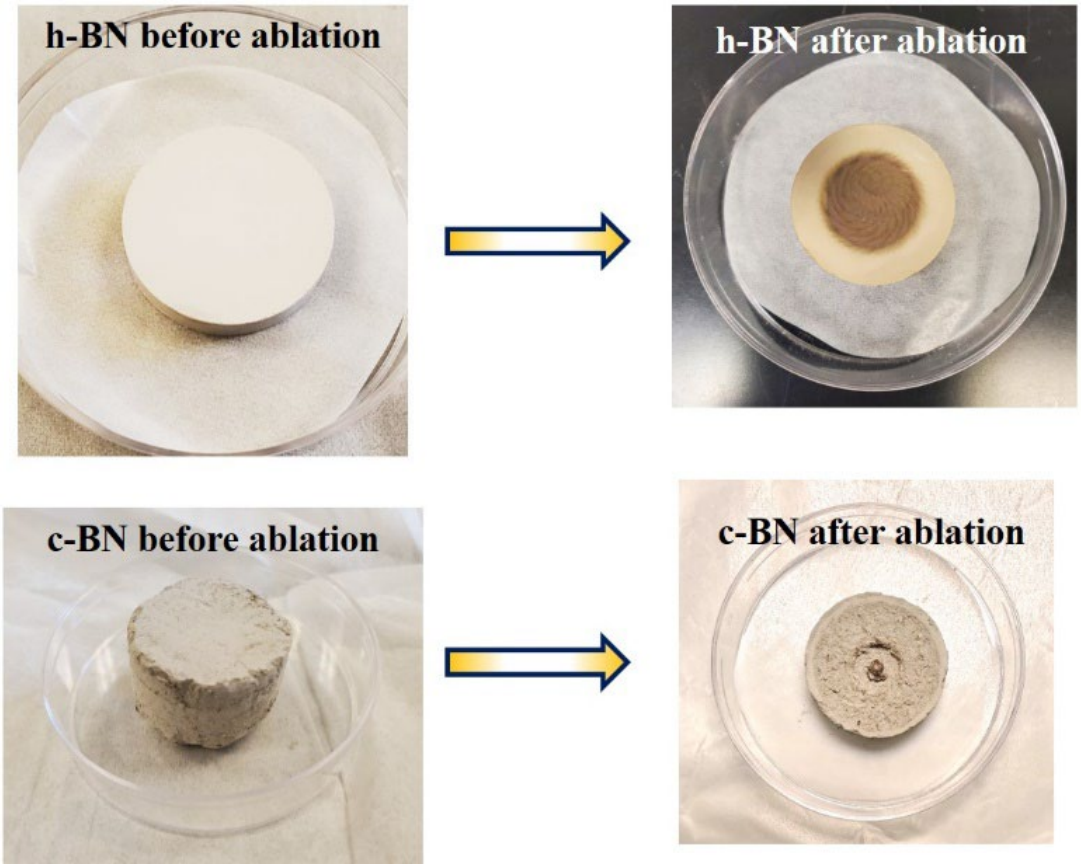

Fig. 11 Photographs of h-BN and c-BN target after the laser ablation

By observing these challenges and difficulties to make a pure c-BN phase pellet, we tried to mix the c-BN and h-BN powder as different weight-percent (wt%) ratio to make the c-BN material containing disk for the laser ablation. Therefore, we made the disk following 25% h-BN + 75% c-BN, 50% h-BN + 50% c-BN, and 75% h-BN + 25% c-BN. We were successful; thus, we further characterized them by using various characterizations. We systematically observed the changes in XRD peak intensity changes while moving from bulk h-BN to c-BN, following the basic principle of Vagard's law. Similar observation has been made to the Raman spectra as well. FESEM shows the 2D sheet and 3D particle-like features for pristine phases; however, for mixed c-BN and h-BN phases we observe the presence of both sheet and particle-like features. For the 50:50 cubic and hexagonal mixed phase we see a broad Raman spectrum, possibly both the emitted spectra made destructive interferences (Fig. 12). FTIR spectra clearly show the absorbance intensity variation of c-BN and h-BN, which correspond to the percentage of phases that exist in each of the mixed-phase composites. Among the mixed-phase materials, we also found that with the increase of c-BN, the density of the pellet decreases and becomes softer. The typical density of 50:50 mixed-phase pellet was 1.3 g/cm^3, whereas for the 75% c-BN and 25% h-BN missed pellet density was less than 1 g/cm^3; hence, the high percentage of c-BN containing pellet remains a soft one.

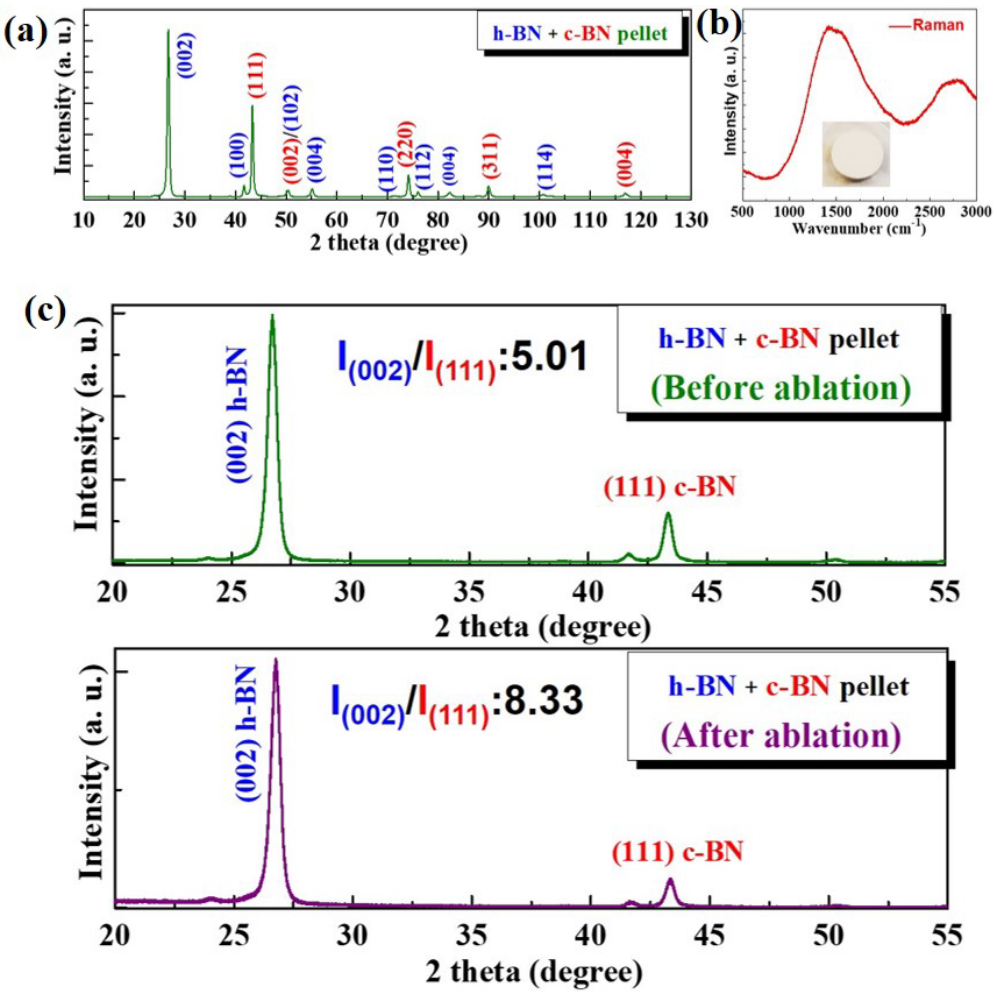

Fig. 12 (a,b) Making of 50:50 h-BN and c-BN composite target material for the deposition. The sintering condition for the pellets was 1000 °C, 12 h in vacuum. (c) Intensity ratio comparison of (002) h-BN and (111) c-BN peaks in the mixed-phase composite pellet, before and after laser ablation.

We have also used the 50:50 h-BN + c-BN mixed-phase pellet for the laser deposition for the c-BN growth, which we discussed later in the thin film characterization section. However, we characterized the mixed-phase composite disk after the laser ablation. As we observed through grazing angle X-ray diffraction (GIXRD), the intensity of ratio of (002) h-BN to (111) c-BN changed from 5.01 to 8.33 for the composite, which indicates that more c-BN materials (containing the ions and radicals) are coming out from that target with laser ablation (Fig. 12).

Since 50:50 h-BN + c-BN mixed-phase composite pellet was reasonable to use as a target for laser ablation, we further investigated its structural, optical, and thermal properties. HPHT plays a crucial role for the stability of polymorphs of BN; therefore, we used a high-temperature spark plasma sintering (SPS) process to this

pellet and observed remarkable changes in its functional properties. Comparative structural analyses of the composite, both pre-SPS (left panel) and post-SPS (right panel) (Fig. 13). Structurally, various analytical techniques including XRD, FESEM, Raman, FTIR, and high-resolution transmission electron microscopy (HRTEM) indicate the exclusive presence of h-BN after SPS. XRD reveals diffraction peaks exclusively corresponding to h-BN. Notably, the quality of h-BN significantly improves post-SPS, evident in the much narrower (0002) h-BN peak with FWHM values of approximately 0.503° (pre-SPS) and 0.303° (post-SPS). Furthermore, after SPS, the Valence Band Maximum (VBM) shifts away from the Fermi level, closely resembling pristine h-BN. FESEM images depict distinctive sheet-like features characteristic of h-BN (Fig. 5b). Raman spectra exhibit solely the h-BN E_{2g} peak at around 1367 cm^{-1}, with a narrow FWHM of approximately 13 cm^{-1}, confirming excellent crystalline quality. This blue shift in Raman spectra post-SPS may be attributed to the hardening of the E_{2g} phonon mode due to shorter B–N bonds induced by pressure during SPS. FTIR analysis also reveals only h-BN-related peaks. Moreover, HRTEM illustrates the presence of sheet-like features corresponding to 2D h-BN. Interestingly, the FWHM of the (002) h-BN peak diminishes following SPS, indicating an enhancement in the crystalline quality of h-BN (Fig. 13).

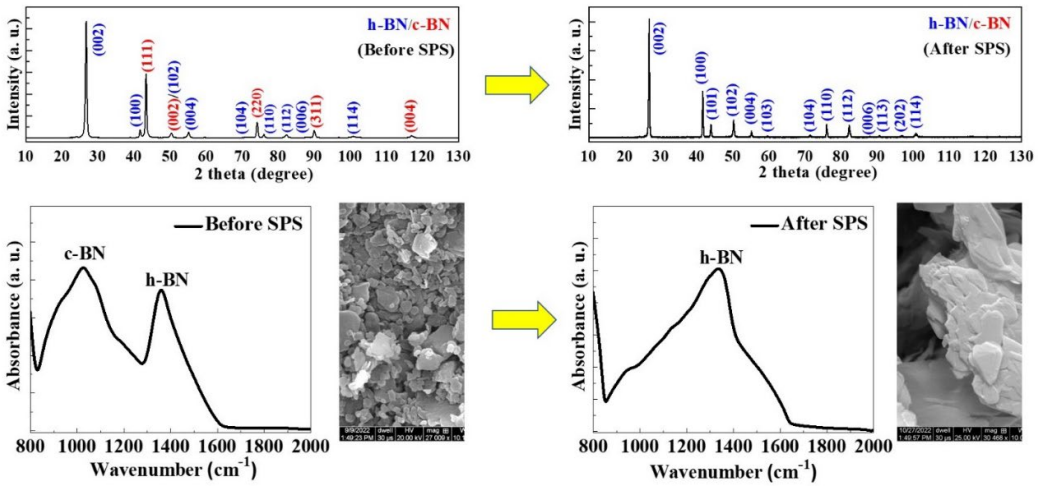

Fig. 13 Characterization of as-made and after spark-plasma-sintered 50:50 mixed phase (c-BN and h-BN) composite, showing the full phase transformation to h-BN, after the SPS process

We conducted a comparison of the Second Harmonic Generation (SHG) yield with pristine c-BN or h-BN powder, both exhibiting SHG response, albeit at an order of magnitude lower than that of the h-BN/c-BN nanocomposite (Fig. 14a). The observed enhancement in SHG from the nanocomposite could be ascribed to the high-temperature annealing process (1000 °C), likely aiding in enhancing crystallinity and leveraging the synergistic effect of the two phases and thereby

effectively boosting SHG efficiency. Consequently, we estimate the lower bound of the effective second-order nonlinear susceptibility $|\chi^{(2)}|$ in the composite to be approximately 3 pm/V, comparable to values observed in typical nonlinear optical crystals; thus, suggesting potential utility in nonlinear optoelectronic applications.

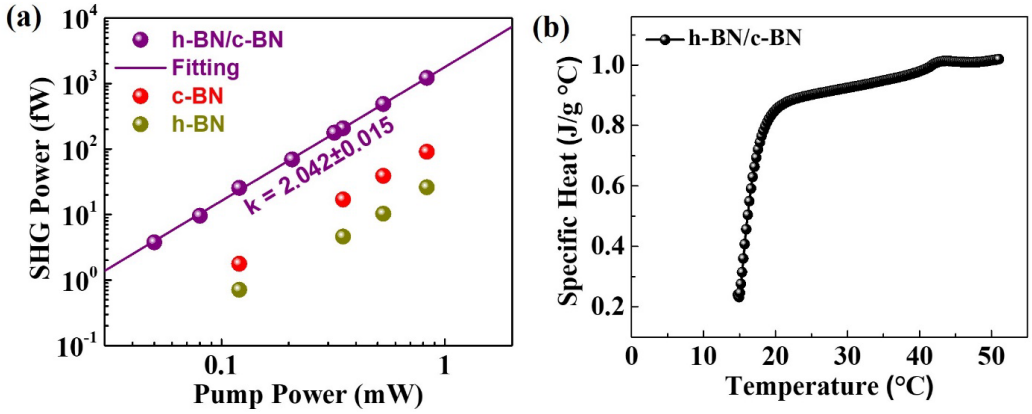

Fig. 14 Optical second harmonic generation and thermal conductivity of h-BN + c-BN mixed-phase composite

The thermal conductivity (k) of BN holds significant relevance across various applications, serving as a pivotal element in heat dissipation or thermal insulation mechanisms. Hence, we determined the RT thermal conductivity (k) of the composite through a comprehensive approach. This involved measuring the thermal diffusivity (α) via the laser flash method, determining the specific heat capacity (Cp) utilizing differential scanning calorimetry, and assessing the density (ρ), subsequently applying the relationship $k = C_p*\rho*\alpha$. The laser flash method data, depicting temperature rise versus time, underwent fitting using the Dusza combined model. The derived values were $\alpha = 0.0135 \pm 0.00056$ cm^2/s, $C_p = 0.903 \pm 0.0135$ J/(g-K), and $\rho = 1.57 \pm 0.007$ g/cm^3, resulting in $k = 1.91 \pm 0.08$ W/(mK) (Fig. 14b). Literature suggests that BN ceramics comprised solely of h-BN exhibit higher thermal conductivity. Notably, this study represents the inaugural assessment of thermal conductivity for a nanocomposite based on BN polymorphs. We attribute the lower thermal conductivity of the nanocomposite to its relatively low density of approximately 57% (calculated as a percentage of the theoretical density of the h-BN/c-BN nanocomposite) and to the thermal resistance existing between the 2D/3D h-BN/c-BN grains. This resistance is further accentuated by the heightened concentration of grain boundaries due to the presence of small c-BN grains. Nevertheless, the modest thermal conductivity holds promise in facilitating the generation and efficient management of thermal energy, functioning as effective thermal insulation. Additionally, it may contribute positively to achieving a high thermoelectric figure of merit in engineered thermoelectric materials based on nanocomposites.

After SPS, the density (ρ) of the nanocomposite also rises to approximately 2.1 ± 0.2 g/cm^3, closely approaching the theoretical value of h-BN, as SPS operates as a HPHT densification process. Additionally, we evaluated the thermal conductivity of the nanocomposite post-SPS, now transformed into h-BN. Utilizing the laser flash method data (temperature rise vs. time), we fitted the results with the Dusza combined model. Through this fitting process, we derived a thermal diffusivity (α) of approximately 0.480 ± 0.0193 cm^2/s. By employing the specific heat capacity (C_p) of h-BN, approximately 0.780 J/(g-K), we calculated RT thermal conductivity (k) to be around 79 ± 0.9 W/(mK). This increase in thermal conductivity after the SPS process could be attributed to both densification and the improved crystallinity of h-BN. The 2D/3D h-BN/c-BN nanocomposite fully transitions to h-BN.

Seeing the complex phase diagram of BN, we also explored the phase stability and phase evaluation by sintering the powder at HPHT by using the SPS process. For the sintering process, we systematically increased the sintering temperature from RT to 2200 °C, by keeping the sintering pressure 90 MPa. When we performed SPS until the temperature reached 1500 °C, and until 1000 °C, c-BN retains the same phase. Whereas, when SPS is performed at more than 1000 to 1500 °C, it transforms to the mixed-phase BN. When the temperature is further raised above 1700 °C, the c-BN powder fully transforms to the high-quality hexagonal phases (Fig. 15). We performed detailed characterizations to confirm the mixed-phase BN. Further, we investigated the properties of phase transformed h-BN.

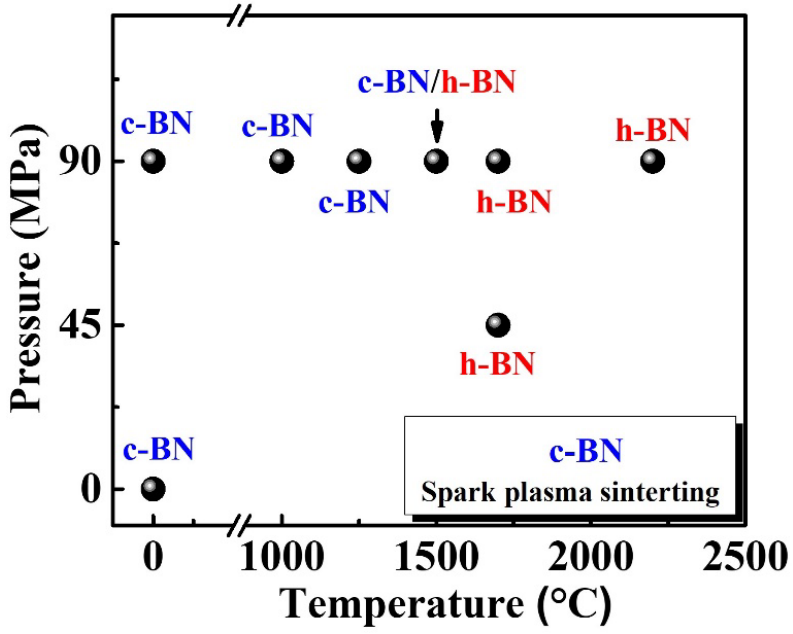

Fig. 15 Spark plasmas sintering phase diagram and phase evolution of c-BN

4.3 Optimization of c-BN Thin Film Growth on (001) SCD

Moving on to the growth of c-BN films, we also tried to optimize the c-BN growth on diamond substrate. In our third-year review, we reported the optimization process as follows:

1) RT growth and in situ annealing
2) High-temperature growth and in situ annealing
3) Pressure-dependent BN growth on SCD at high temperature
4) Frequency-dependent BN growth on SCD at high temperature
5) Doping-dependent BN growth on SCD at high temperature (Mg and Si)
6) BN growth on implanted SCD surface

All of these analyses showed the formation of amorphous-phase BN on (001) single-crystal substrates. Therefore, we continued to pursue the optimization process in search of epitaxial c-BN growth. In 2024, we also adopted various growth conditions to enhance the quality of c-BN film on diamond substrate as described below.

4.3.1 Distance Dependent Growth at Low Pressure

In 2023, we speculated that the low energy growth kinetics might be favorable for the growth of c-BN. To validate this, we varied the target-to-substrate distance systematically and grew the films at a low partial pressure of 1 mTorr. We have grown three films by varying the distance from 50 to 60 mm, and up to 70 mm. After the growth, we took out the sample from the chamber and performed the XRD, XPS, Raman spectroscopy, and FTIR spectroscopy (Fig. 16). The XPS showed the presence of B and N in all the samples (Fig. 16a and 16b). Since we used low partial pressure, the samples contain some amount of nitrogen vacancies, the B:N ratio in XPS was also found to vary with distance. Raman and FTIR spectroscopy showed the presence of both cubic and hexagonal phases (Fig. 16c and 16d). We also performed GIXRD of the sample, which showed the presence of c-BN peak; however, we did not observe any h-BN related peak in GIXRD (Fig. 16e and 16f). From the growth conditions, we concluded that varying the distance and more importantly applying low partial pressure during the growth is not adequate to grow the c-BN phase.

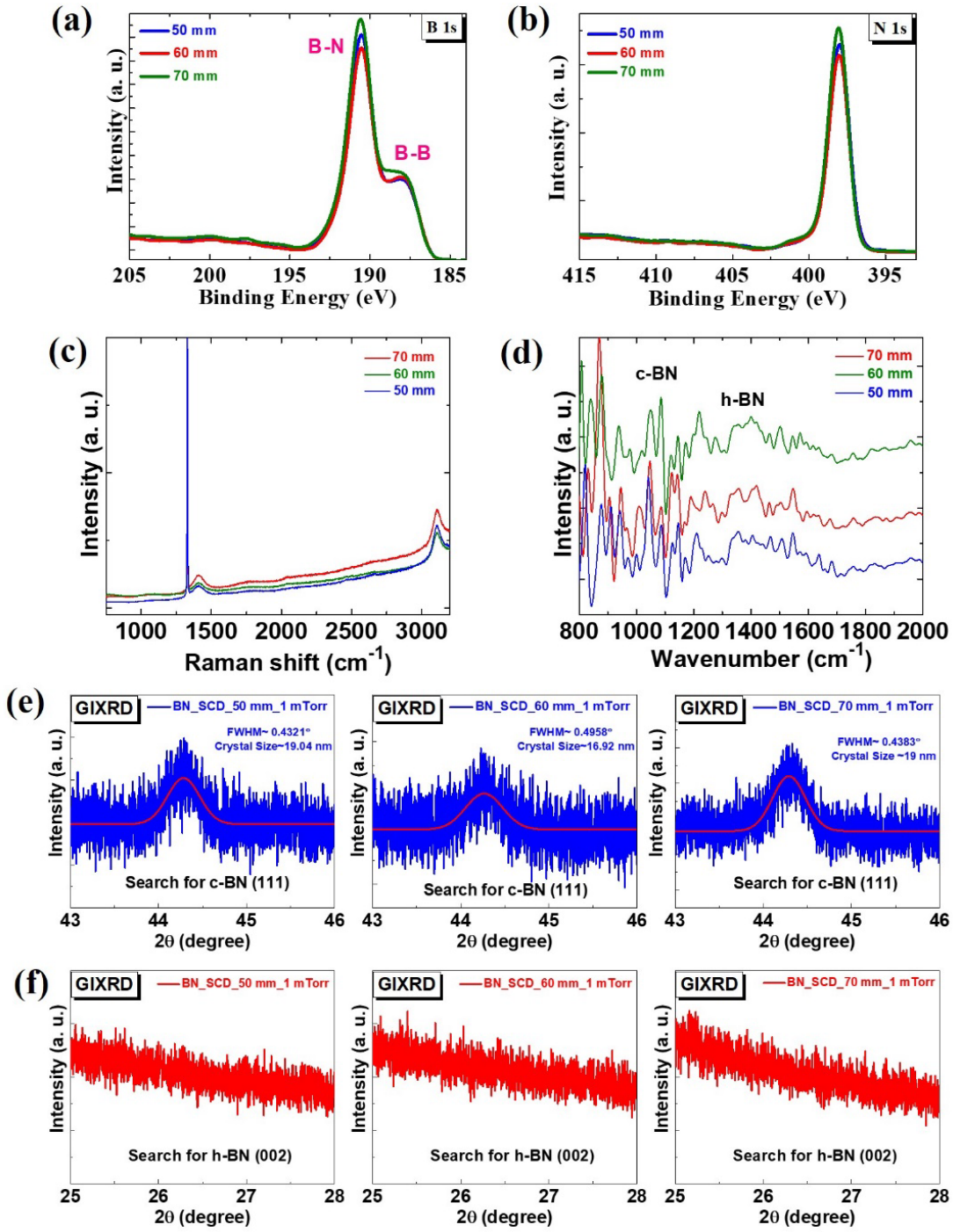

Fig. 16 (a) XPS, (b) Raman spectra, (c) FTIR spectroscopy, and (e,f) grazing-angle XRD of the BN films grown at high temperature and low pressure with varying target-to-substrate.

4.3.2 Growth on Hydrogenated and Nitrogen Functionalized Diamond Surface and Monitoring the Growth using RHEED

In literature it has been shown (mainly in theoretical calculations) that, instead of pristine diamond surface, functionalized diamond surface helps promote the nucleation of c-BN growth. Proper surface preparation and employing nucleation layers is essential for facilitating adhesion and the continuous growth of c-BN films. It is believed that a nitrogen functionalized SCD surface is pivotal to the initial epitaxial growth of thin c-BN films, as evidenced by calculations indicating the strongest interfacial binding energy for nitrogenated (001) SCD surfaces. Functionalization introduces active sites on the SCD surface, fostering c-BN nucleation and facilitating the formation of robust bonds between the substrate and film. Augmented adhesion is crucial to forestall delamination and ensure film stability during growth. Functionalization can alter the surface structure to mitigate lattice mismatch with c-BN, enhancing crystallographic alignment and overall film quality. It also enables the adjustment of surface energy and reconstruction, influencing precursor wetting behavior during deposition and promoting superior coverage and uniformity of c-BN films. Moreover, functionalization fosters the creation of a chemically compatible interface between SCD and c-BN, imperative for achieving high-quality interfaces. It also enables the optimization of the surface for specific growth conditions such as temperature and pressure, which are necessary for c-BN deposition. Thus, a functionalized SCD surface is integral to the successful growth of c-BN thin films.

Therefore, we have grown films on three different (001) SCD substrates; namely, pristine SCD, hydrogenated SCD, and nitrogenated SCD surfaces. Initially, SCD was subjected to an acid wash (H_2SO_4 + HNO_3, in a 3:1 volume ratio) to remove surface contaminants. Then, a hydrogen (H_2) plasma treatment was conducted within the diamond growth chamber to hydrogenate the diamond surface. Subsequently, the hydrogenated SCD underwent treatment with hydrobromic acid to induce partial surface oxidation. The nitrogenation process was then performed using a home-built UV-irradiation setup in an ammonia (NH_3) gas environment to yield N-SCD. Details of the nitrogenation procedure are available in a previous report.[12] To validate the presence of nitrogen on the SCD surface, XPS analysis was conducted. The XPS survey scan revealed a minor nitrogen peak at approximately 400 eV (Fig. 1a), constituting roughly 3% of the surface composition (Fig. 17). We have grown the samples at 550 °C and 50 mTorr N_2 partials pressure. We provided 2000 shots at 5 Hz for the deposition. First, we characterized the substrate surfaces by using the reflection high-energy electron diffraction (RHEED). RHEED is a powerful technique used in the study of surfaces, thin films, and interfaces of crystalline materials. It uses a beam of high-energy electrons, typically in the range

of tens of kiloelectronvolts, which are directed onto the surface of a sample at a very shallow angle of incidence, typically less than 1°.

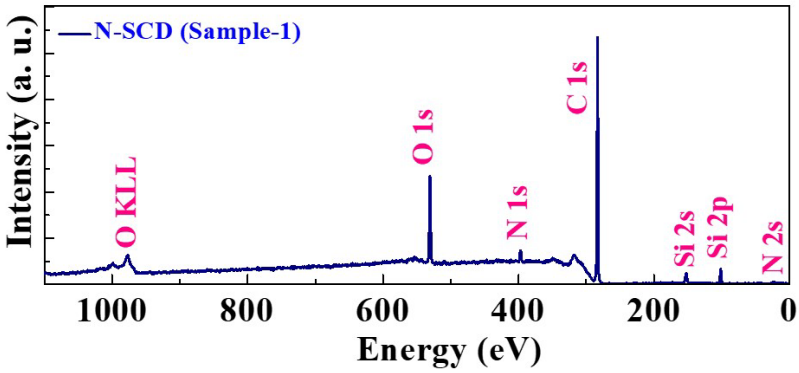

C	63.5
O	25.0
Si	8.5
N	3.0

Fig. 17 Nitrogen functionalized diamond surface showing the presence of 3% nitrogen on the diamond surface

The interaction between the electrons and the atoms in the sample surface results in various scattering processes, including elastic scattering, inelastic scattering, and diffraction. The diffraction patterns produced by RHEED arise from the periodic arrangement of atoms in the crystalline lattice of the sample. These diffraction patterns contain valuable information about the surface structure, symmetry, orientation, and quality of the crystalline material. RHEED is particularly useful for monitoring the growth of thin films and epitaxial layers in real time during the deposition processes (e.g., molecular beam epitaxy [MBE] and CVD). By analyzing changes in the intensity, position, and shape of the diffraction patterns, researchers can gain insights into the growth dynamics, crystalline quality, and surface morphology of the growing film. Moreover, RHEED can also be employed for surface characterization, surface reconstruction studies, and in situ monitoring of surface processes such as surface diffusion and surface reactions. Overall, RHEED is a versatile and nondestructive technique that provides valuable information about the structural properties of crystalline surfaces and thin films, making it an essential tool in materials science and surface physics research.

As seen from the diffraction pattern, the surface reconstruction has changed due to N terminations, which are supposed to modify the growth of c-BN (Fig. 18a). Next, we tried to analyze the growth pattern by monitoring the RHEED intensity during the growth of the BN layer. We observed that the intensity started decaying during the growth, possibly due to the lattice mismatch and nonepitaxial nature of the films with a rough surface (Fig. 18b). After the growth of 20-nm BN, the RHEED intensity oscillation totally vanishes, as seen in the absence of the diffraction spots on Fig. 18c. From RHEED monitoring, it seems the surface of the film is not atomically smooth. In a rough surface, the lattice periodicity is disrupted, leading

to incoherent scattering instead of coherent diffraction. As a result, the diffraction pattern becomes severely distorted, or completely obscured. Electrons penetrating the surface of a rough material encounter multiple scattering events with various surface features (i.e., steps, kinks, and vacancies). These interactions disrupt the coherent diffraction process, leading to a loss of intensity and distortion of the diffraction pattern. The presence of surface roughness leads to a broadening of diffraction peaks. In RHEED, sharp, well-defined peaks are indicative of a highly ordered surface. The broadened peaks, lack of sharp features, and features of rough surfaces, make it difficult to discern any meaningful diffraction pattern.

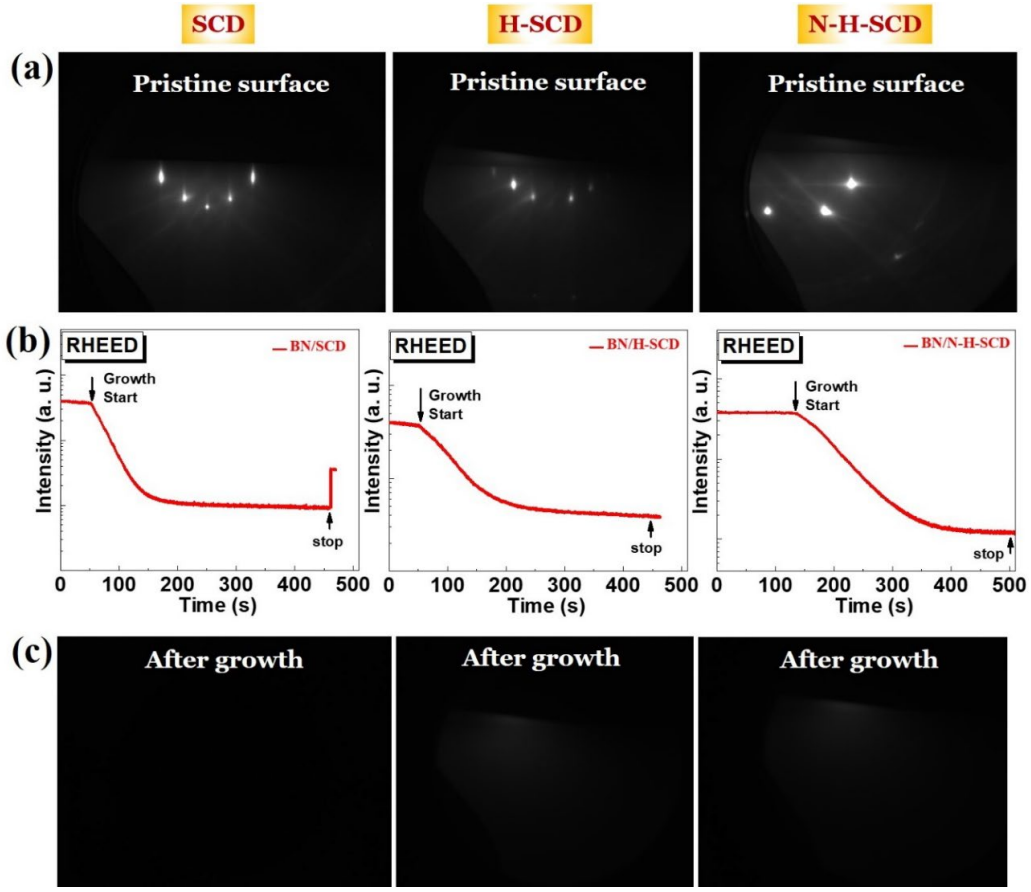

Fig. 18 (a) RHEED diffraction pattern of modified diamond surfaces. (b) RHEED oscillation during the growth monitoring. (c) RHEED diffraction pattern after growth.

Following the growth process, we extracted the sample from the chamber and conducted XRD, XPS, and Raman spectroscopy; XPS analysis revealed the presence of both B and N in all samples (Fig. 19a and 19b). The use of high partial pressure makes the nitrogen vacancies disappear, as we observed for the low-pressure growth case. Consequently, the B:N ratio in XPS exhibited an almost 1:1 ratio. In Raman spectroscopy, we clearly observed the presence of c-BN phase for the nitrogen functionalized surface; however, this was along with trace hexagonal

phase (Fig. 19c). Additionally, GIXRD analysis demonstrated the presence of a c-BN peak, but no h-BN–related peak was observed (Fig. 19d and 19e). Based on the growth conditions, we concluded that functionalization of diamond surfaces helps to promote the formation of the c-BN phase.

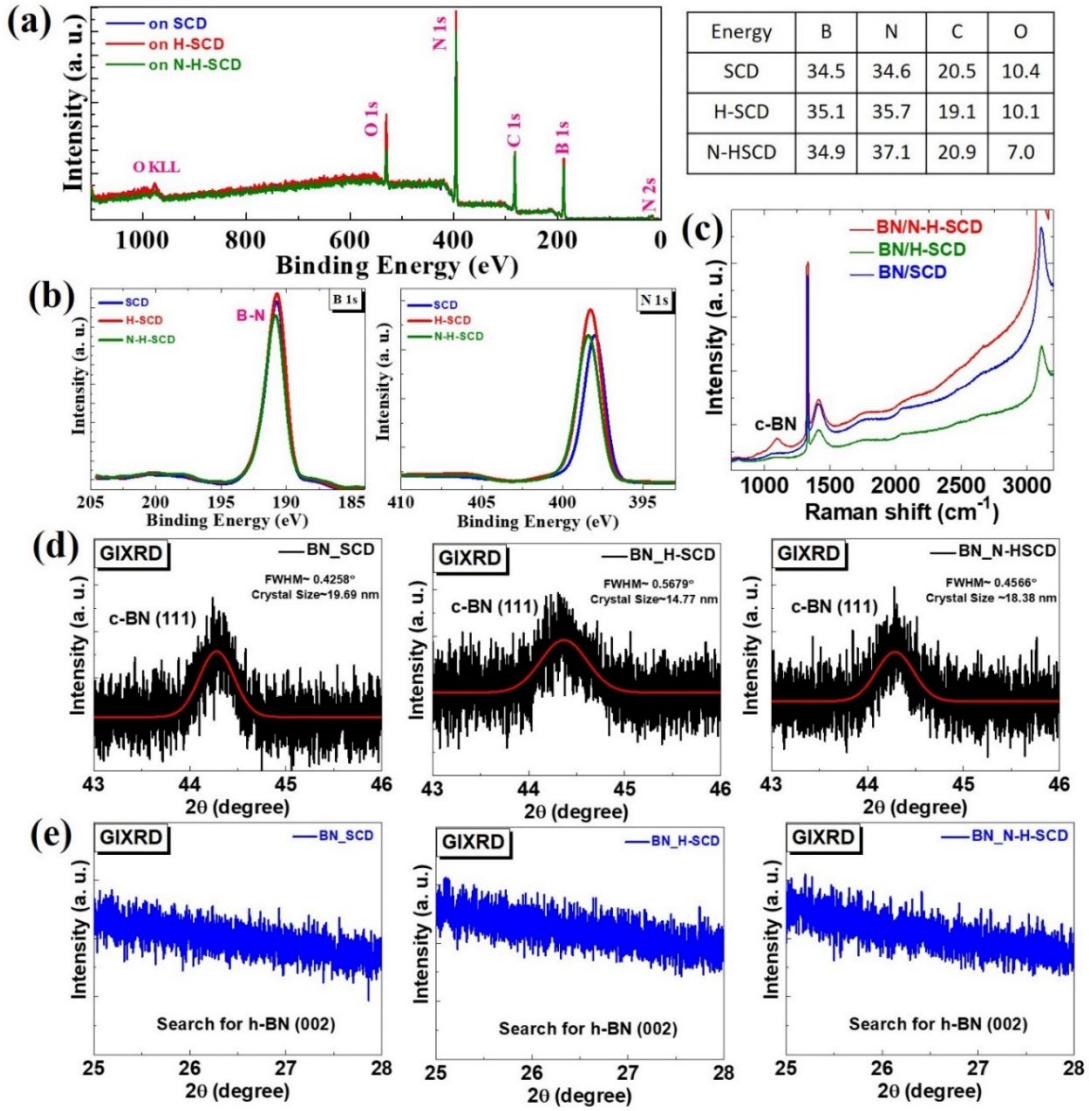

Energy	B	N	C	O
SCD	34.5	34.6	20.5	10.4
H-SCD	35.1	35.7	19.1	10.1
N-HSCD	34.9	37.1	20.9	7.0

Fig. 19 (a,b) XPS, (c) Raman spectra, and (d,e) grazing-angle XRD of the BN films grown at HPHT with a modified diamond surface

4.3.3 Growth on Nitrogen Functionalized Diamond Surface at Lower Growth Temperature and Varying Pressure

As seen in Section 4.3.2, functionalization of (001) SCD helps to promote the c-BN growth. Therefore, we tried to optimize the c-BN growth by lowering the growth temperature to 500 °C and changing the pressure. Thus, we applied two different partial pressures of 100 and 1 mTorr during the growth. As seen in XPS, both films show B–N bonding; however, the films grown at a lower partial pressure show additional B–B peak (Fig. 20a). The film grown at 100-mTorr partial pressure shows an approximately 1:1 B:N ratio, confirming the stoichiometric nature of the grown film. In addition, the π-plasmon peaks also appear in XPS. In XRD, we see c-BN (111) peak for both films; however, the peak intensity of films grown at 100 mTorr shows higher intensity (Fig. 20b). Interestingly, in Raman spectra, only the films grown at 100-mTorr pressure show the signature of c-BN (Fig. 20c). FTIR also shows a higher percentage of c-BN signal for both films (Fig. 20d)—however, this is with the mixed-phase BN. These observations confirm that lower temperature (500 °C) and 100-mTorr growth is more favorable for relatively crystal-like c-BN film growth.

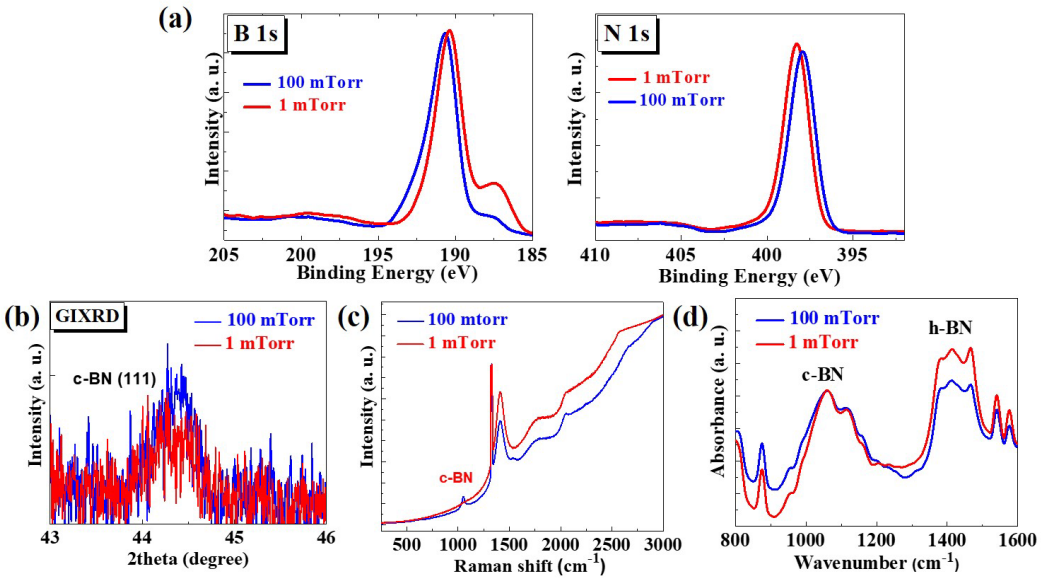

Fig. 20 (a,b) XPS, (b) grazing-angle XRD, (c) Raman spectroscopy, and (d) FTIR spectroscopy of the BN films grown at 500 °C and high and low pressure with a nitrogen-modified diamond surface

After growing the better-quality c-BN film on (001) SCD, we looked through cross-sectional HRTEM to confirm the atomic structure, phases, and crystallinity of the BN/diamond interface. After the focused ion beam (FIB) milling, the interface is analyzed under a microscope to observe the presence of c-BN phase with clean interface between the c-BN and diamond. This has further been confirmed by

diffraction pattern and electron energy loss spectroscopy (EELS) analyses. In addition to the c-BN phase, the top surface also shows a thin layer of amorphous or h-BN (Fig. 21a). This has also been confirmed by presence of π-plasmon peak in the EELS pattern (Fig. 21e). In literature,[13] it has been calculated that on diamond, c-BN can form a uniform layer up to 10–12 layers (~3 nm), and then the subsequent growth follows the a-BN layer. Therefore, our observations follow the important theoretical findings of an ultra-thin uniform layer of c-BN.

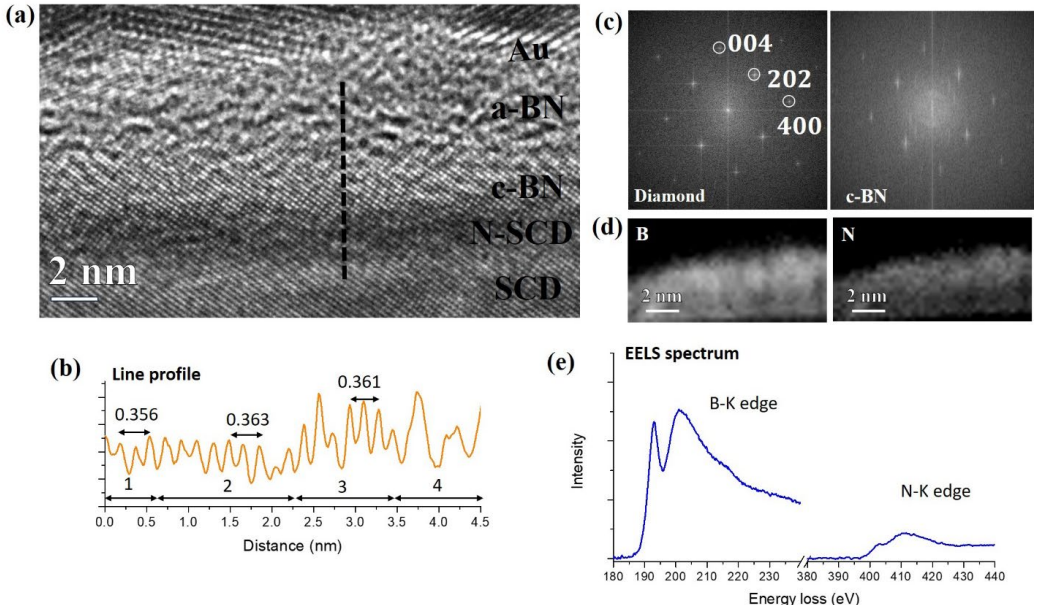

Fig. 21 HRTEM of the BN/diamond film. (a) Cross-sectional image, (b) line profile across the interface, (c) diffraction pattern, (d) EDS of the BN regions (B and N), and (e) EELS spectrum of the BN region showing the presence of atomic ordering of c-BN.

In previous theoretical studies,[13] the layer-by-layer formation of c-BN on diamond (100) was meticulously investigated using quantum mechanical density functional theory (DFT). The study delved into the fundamental requirements for the initial growth of c-BN (100) by sequentially adding alternate B and N layers and assessing the resulting interfacial binding strengths and geometric configurations. Notably, nitrogen heteroepitaxial positioned on diamond (100) exhibited the strongest interfacial binding energy among the monatomic layer configurations. However, individual atoms in a monatomic B adlayer did not adopt corresponding heteroepitaxial positions. The heteroepitaxial adlayer structure remained cubic following geometry optimization when N was attached to the diamond substrate; however, the alternative B-terminated structure exhibited an amorphous-like arrangement, albeit with substantial interfacial binding strength. Interestingly, a two-layer BN structure with B-terminated to the diamond surface only maintained stability in the initial heteroepitaxial lattice configuration, retaining its cubic form

with significant interfacial binding strength. (A connection with the observed experimental data is missing.)

4.3.4 Pulsed Interval Deposition (PID) at Lower Growth Temperature

After confirming the N-functionalized diamond surface and lower temperature can facilitate the c-BN growth, but only near the interface, we explored other growth approaches such as the PID growth process. This process is expected to extend the growth of c-BN process and grow thicker epitaxial c-BN films. In the PLD process, the intense energy of the laser vaporizes the target material, creating a plasma plume composed of atoms, ions, and clusters of the target material. The plasma plume is then directed toward the substrate, where the atoms and clusters condense to form a thin film. The controlled intervals between laser pulses allow for precise control over the deposition process—more precisely, the crystallization process by providing additional thermal energy at the surface, influencing factors such as film thickness, morphology, and crystallinity.

After the growth at films by supplying 2000 laser pulses at three different PID growth processes (5-, 15- and 30-min growth interval after each 250 shots) we characterized the films using XPS, GIXRD, and Raman spectroscopy. Different time intervals provided different amounts of time for crystallizations. The XPS analysis shows the presence of B–N bonding in XPS with πι-plasmon peak at 9 eV apart (Fig. 22a). The GIXRD of the samples show the presence of c-BN (111) peak in the XRD. We also investigated the existence of the h-BN (002) peak in the spectrum, but did not observe any peak related to the h-BN (Fig. 22c). From GIXRD FHWM, we calculated the grain size of 15–20 nm. However, in the Raman spectra of c-BN we observed significant changes; the films annealed for the 5-min PID case, showing intense c-BN TO modes (Fig. 22d). In the Raman spectra, we also observed additional nitrogen vacancy (NV^-) related peaks. These observations show that using a 5-min PID deposition at a lower growth temperature (500 °C) shows growth of good-quality c-BN on the (001) SCD surface.

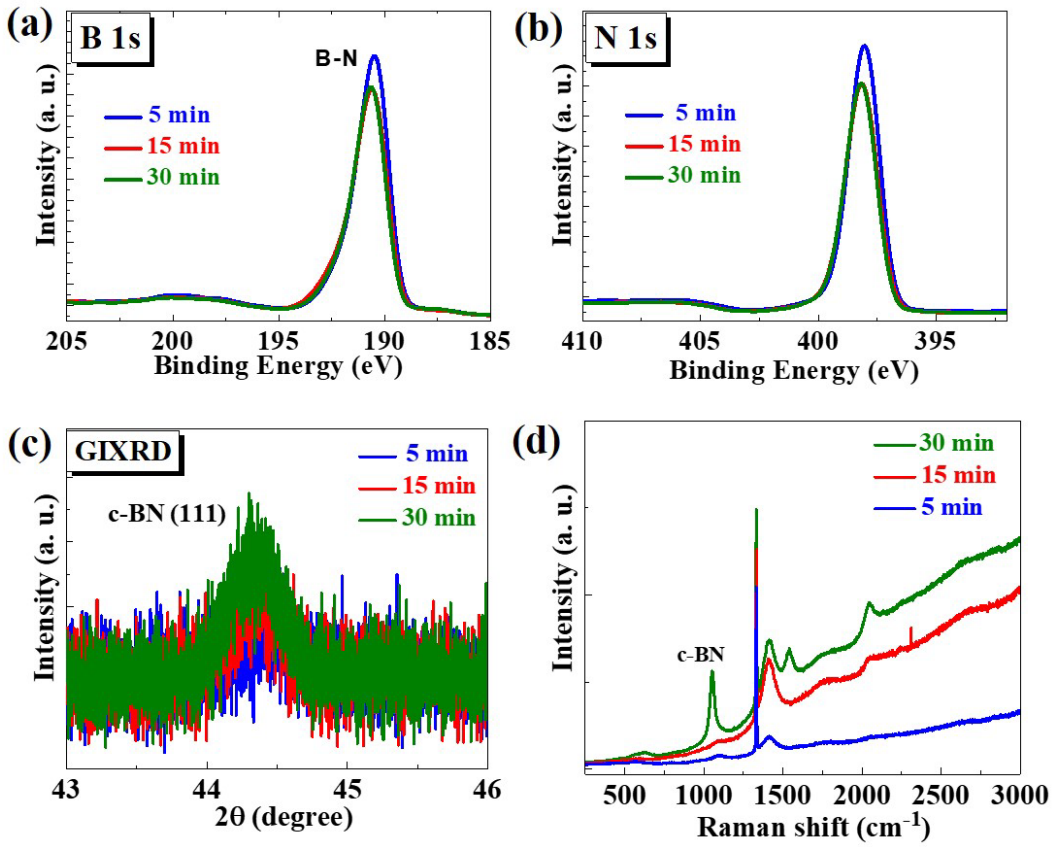

Fig. 22 (a,b) XPS, (c) grazing-angle XRD, and (d) Raman spectroscopy of the BN films grown at 500 °C by using PID deposition by varying the interval time

4.3.5 PID at Varying the Target-to-Substrate Distance

Varying the target-to-substrate distance in PID in the PLD growth processes can have significant impact on the resulting thin film properties. Adjusting the target-to-substrate distance can also help both the control of the deposition rate of the material onto the substrate and the flux of ablated material reaching the substrate surface. This control is crucial for achieving the desired thickness and uniformity of the deposited film by modulating the kinetic energy of the ablated species arriving at the substrate surface. Proper adjustment of the target-to-substrate distance is crucial for minimizing defects such as voids, cracks, and surface roughness in the deposited thin films; hence, increasing the quality of the crystal. Therefore, we varied the target-to-substrate distance from 50, 55, and 60 mm, while keeping all other growth conditions like those used previously. As seen, XPS films show the presence of B and N, with an approximately 1:1 atomic ratio (Fig. 23a and 23b). However, when we move away from the film, the B–N peaks reveal that a lesser amount of N is making its way to the substrate since the traveling distance for those atoms or molecules depend on the kinetic energy of the respective ions.

Further characterizations using GIXRD show the presence of c-BN (111) peak. Interestingly, for longer target-to-substrate distances, the c-BN peak in Raman spectra as well as in FTIR spectra show diminishing trends. These observations suggest that PID growth at 550 °C, 100-mTorr partial pressure, and 50-mm distance is better for the c-BN.

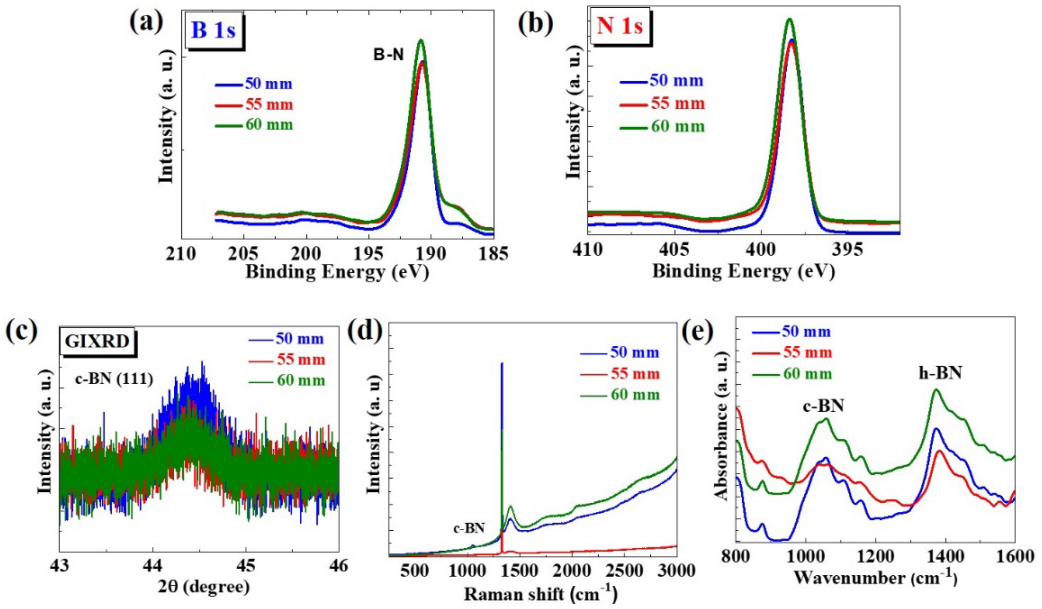

Fig. 23 (a,b) XPS, (c) grazing-angle XRD, (d) Raman spectroscopy, and (e) FTIR spectroscopy of the BN films grown at 500 °C using PID deposition by varying the target-to-substrate distance

4.3.6 PID Growth of c-BN on HPHT Diamond

Apart from E6-SCD, we also used HPHT diamond substrate (supplied by ARL) to grow c-BN. After obtaining the HPHT diamond, we characterized the diamond surfaces by using conventional techniques. XRD of the diamond surface shows only (004) peak with very sharp FWHM, confirming the high crystallinity (Fig. 24a). We also investigated the miscut angle of the HPHT diamond by doing the XRD rocking curve measurement at a different azimuthal angle. As seen from the rocking curves, the miscut angle of the HPHT diamond is approximately 1° (Fig. 24b), which is much lower than the E6-SCD (~2°–3°). The XPS survey scan on the HPHT diamond shows intense peak with small traces of N-peak. Raman spectroscopy of the HPHT substrates shows the highly intense diamond D-band peak, without any trace of N-vacancy peaks, which was generally observed for the E6-SCD case. We also performed acid wash (using CF_6) of the HPHT surface in a clean room to clean the surface as well as remove the oxygen-related species or contaminants on any of the HPHT surfaces.

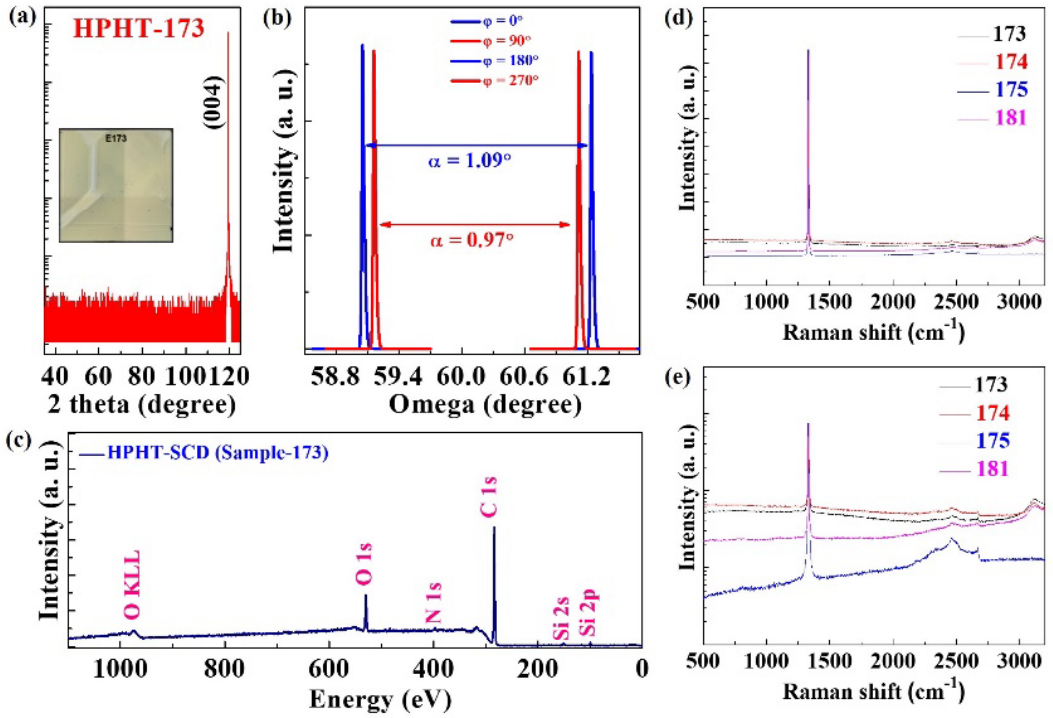

Fig. 24 (a,b) XRD and miscut angle, (c) XPS, (d,e) Raman spectroscopy and its zoomed-in version of the HPHT diamond

After treating the HPHT diamond surfaces, c-BN growth was attempted using the PID growth approach (i.e., 5-min interval after each 250 shots deposition), repetition 1 Hz, growth temperature 450 or 500 °C, target-to-substrate distance of 50 mm, laser energy of 2.2. J/cm^2, and pre-and post-annealing of 30 min at the same growth temperature and pressure. In total, we supplied 2000 laser shots for the ablation. After growth, we took out the samples and characterized them by using the XPS, XRD, Raman spectroscopy, and FTIR spectroscopy. As observed in the XPS analysis, all samples exhibited the presence of both B and N elements (Fig. 25a). Consequently, the B:N ratio, as determined by XPS, exhibited an approximately 1:1 elemental ratio. However, we observed the plasmons peak in the XPS. GIXRD analysis revealed the presence of a c-BN peak; however, no discernible peak associated with hexagonal-BN was observed (Fig. 25c). Additionally, Raman and FTIR spectroscopy confirmed the existence of both cubic and hexagonal phases (Fig. 25d and 25e). Therefore, BN films grown on HPHT diamond shows the formation of c-BN phase, with some trace of h-BN phase.

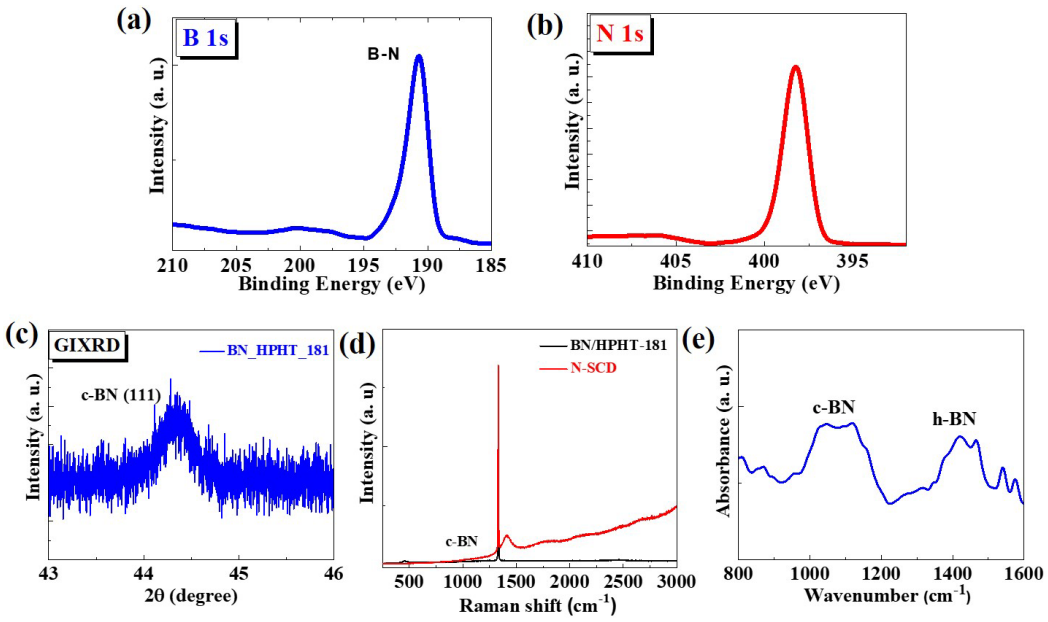

Fig. 25 (a,b) XPS, (c) grazing-angle XRD, (d) Raman spectroscopy, and (e) FTIR spectroscopy of the BN films grown on HPHT diamond

4.3.7 Raman Spectroscopy Comparison of Pristine Diamond and Grown BN Films

We compared the Raman spectra of nitrogen functionalized (001) SCD, HPHT diamond, and BN films grown on both the substrates with bulk c-BN powder. As seen, bulk c-BN shows TO and LO modes at 1054 cm^{-1} and 1304 cm^{-1}. N-SCD shows the diamond D-band peak with an NV^0 center peak. In contrast, HPHT diamond shows only the diamond D-band peak without any vacancies. Films grown on the E6 N-SCD sample show the c-BN TO modes, like those of the bulk c-BN case; however, the NV^0 peak remains in the heterostructure (Fig. 26). BN films grown on HPHT substrate at two different temperatures also show the c-BN peaks without any NV^0 peak. However, for BN grown on HPHT, the Raman mode was blue shifted, possibly due to the different grain sizes and surface morphologies. In conclusion, BN on N-SCD shows an excellent c-BN peak; however, with N-vacancies BN grown on HPHT diamond shows only the c-BN peak (without any vacancies) but still slightly shifted from the bulk c-BN peak.

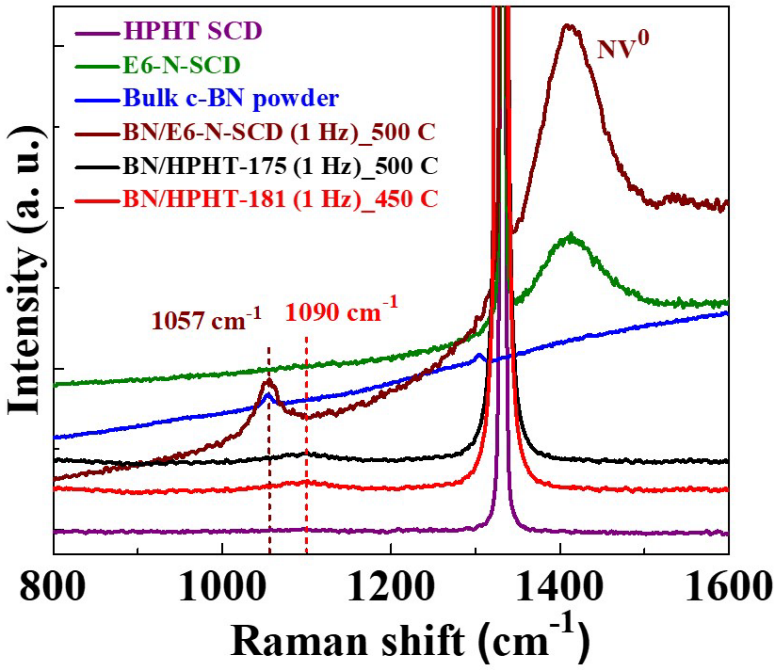

Fig. 26 (a) Raman spectroscopy comparison of pristine E6-(001) SCD, HPHT diamond, bulk c-BN, and BN thin films grown on E6-SCD and HPHT diamonds

4.4 Conclusion and Future Plan

We made several efforts to optimize and grow high-quality c-BN thin films on single-crystal (001) diamond substrates. Our methods involved adjusting growth temperature, partial pressure, laser parameters, repetition rates, elemental doping, N-functionalization, and cation implantation on diamond surfaces to comprehensively understand and refine the growth process of c-BN thin films. Through our experiments we found that achieving superior crystalline c-BN films necessitates specific growth conditions; namely, a temperature of 500 °C and a nitrogen pressure of approximately 100 mTorr for c-BN thin film deposition on N-SCD surfaces, albeit primarily favoring the growth of the most stable c-BN (111) phase. Additionally, we observed significant enhancements in c-BN growth through N-functionalization of the SCD surface, underscoring the critical role of surface modification in facilitating BN growth. Looking ahead, we intend to manipulate nitrogen concentration on the SCD surface using both wet and dry chemistry techniques to disrupt diamond surface reconstruction and further encourage c-BN growth. Ultimately, by refining these parameters and exerting tighter control overgrowth conditions, we aim to realize atomically smooth, defect-free, pure, and doped (001) c-BN thin films on (001) diamond surfaces, which is crucial for the development of future diamond-based RF devices.

5. Transmission Electron Microscopy (TEM) Characterization of Single-Crystalline Diamond Substrates and c-BN/Diamond Interfaces

One of the most powerful techniques to investigate the nanometer-scale interfaces between SCD and BN in amorphous (a-C), cubic (c-BN), or hexagonal (h-BN) phases is TEM. We used the following microscopes for TEM analysis: Rice University's Titan Themis[3] (at 300 kV) and Oak Ridge National Laboratory's (ORNL's) UltraSTEM 100 (at 60 and 100 kV). Possibilities of Titan allowed us to 1) demonstrate and analyze the crystalline structures of c-BN on SCD, 2) determine the existence of both h- and c-BN phases at a phase transition point, and 3) conduct in situ heating experiments on c-BN. Chemical composition of the samples was determined using electron dispersive X-ray spectroscopy (EDX), while additional information about phases and electron bonding was determined using electron energy loss spectroscopy (EELS) both on Titan and UltraSTEM 100. Initial information about BN phases and orientation determination of micro-/nanoparticles was done via selected area electron diffraction (SAED). To investigate the BN/diamond interface, a cross section of lamella was cut out from the bulk of the sample using FIB at 30 kV and thinned at 5 kV for precision.

We worked with the following samples that were either grown at Rice University or sent to us from ARL:

- Pristine c-BN powder, deposited on the e-chips, for conducting the in situ heating experiments.
- The c-BN powder that was treated by SPS (1500 °C and 90 MPa).
- Nitrogen-functionalized SCD with PLD deposited BN (500 °C, 2000 shots, 100 μTorr).
- HPHT diamond substrate acid washed with CF6 with PLD deposited BN (500 °C, 250/2000 shots, 100 μTorr).
- Carbon ion-implanted diamond sample with 1.5-h epilayer that has a-C layer in between.
- Carbon ion-implanted diamond sample with 2-h epilayer that has graphite layer in between.
- BN was grown on SCD using microwave-plasma chemical vapor deposition (MPCVD) at 920 °C with H_2/N_2 gases and ammonia borane as precursor.

5.1 Investigation of h-BN/c-BN Phase Transition by In Situ Heating

To investigate the phase transition of c-BN into h-BN, in situ TEM heating experiments were conducted on the pristine c-BN powder. The c-BN powder was dissolved in isopropyl alcohol (IPA) solution and sonicated for reducing the agglomeration of c-BN particles. A drop of the solution was deposited on the e-chip via pipette, after which the chip was baked on the hot plate for 30 min at 130° C. The sample preparation and the schematic of the e-chip is shown on Fig. 27a–27d. We noticed that after deposition and baking, c-BN particles started to agglomerate around the holes in the e-chip membrane, which proved a considerable problem during the TEM imaging and analysis (Fig. 1b). The size of the particles after sonication is from 0.5 to 2.0 microns, which is too thick for proper TEM imaging (Fig. 1c). Open areas seen on Fig. 1e are almost nonexistent and even there the c-BN particles tend to form stable structures. The phase and orientation of the c-BN particles can be determined from SAED as seen from Fig. 1f, where we can see the first-order spots that represent the (111) orientation of the c-BN particle.

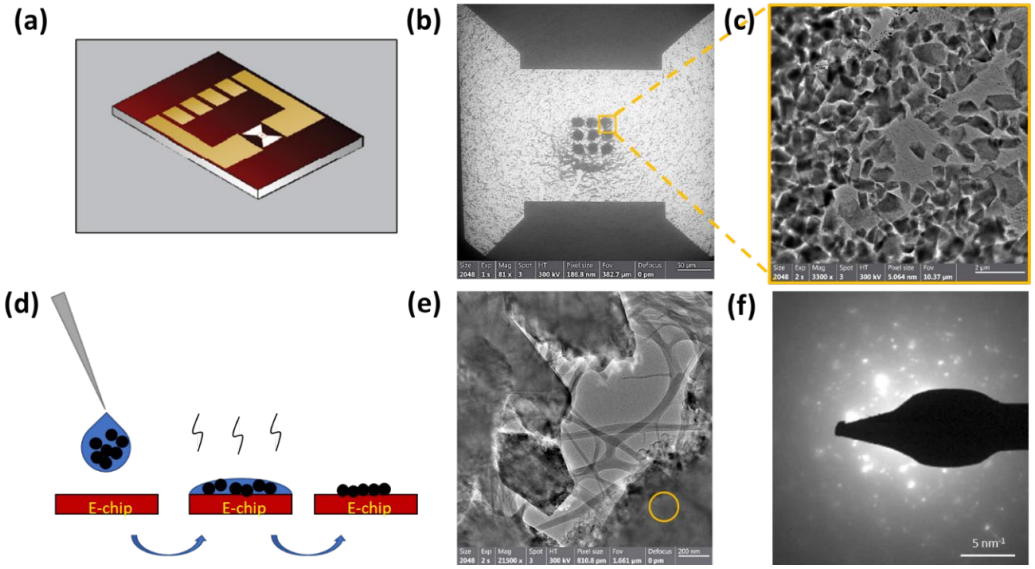

Fig. 27 Sample preparation and TEM analysis during in situ heating experiment. (a) Schematic of the heating e-chip, (b) TEM image of the membrane on the e-chip after depositing the c-BN solution, (c) Magnified region of interest on the e-chip with c-BN particles, (d) drop-casting technique of sample preparation, (e) close-up TEM image of the c-BN particles with yellow circle denoting the area for the electron diffraction in f, (f) SAED showing the (111) orientation of the c-BN particle

SAED from the c-BN particle has multiple spots that do not belong to this particle. They come from the ceramic heating membrane of the e-chip and other particles that are located under the one seen in the yellow circle on Fig. 1e.

Heating was done in several steps:

1) RT to 350 °C, increasing temperature by 8 °C every second.
2) RT of 350–1000 °C, increasing temperature by 8 °C every second.
3) RT of 1000–1200 °C, increasing temperature by 1 °C every second.

During the change of temperature at each step of the heating, the possible phase of one of the particles was monitored via diffraction pattern since high-resolution atomic imaging was not possible due to the thickness of the sample. No changes of the phase were observed at any stage of heating. The particles started to move around their locations as well as migrating to different places as the temperature increased.

5.2 Cubic and Hexagonal BN phases and Phase Boundaries

Further experiments regarding phase transitions of c-BN to h-BN and vice versa were conducted using c-BN treated with SPS at 1500 °C. This time the SPS treatment was not done under high vacuum conditions of the electron microscope column chamber, but at high pressures of 90 MPa. Similarly, we dissolved the c-BN/h-BN powder in the IPA solution and after sonication drop-casted it on the TEM grid. Further baking ensured the better attachment of particles to the carbon layer on top of the TEM grid.

The existence of both phases can be seen from large scales of particles (Fig. 28a) since one has a hexagonal shape, while the other has a rectangular shape. After conducting SAED on both the particles (white circles on Fig. 28b), we calculated the angles and ratios of distances between the spots to determine the phases. These numbers from diffraction patterns were compared (Fig. 2c and 2d) with simulations from the Materials Project website* to determine the orientation of each particle. We determined that that square-shaped particle has the (110) orientation of c-BN, while the hexagonal-shaped particle is h-BN, oriented along the $(10\bar{1}0)$. These results—although not typical—are not unusual because after sonication and drop-casting the BN particles can land on the TEM grid in arbitrary orientations. The existence of both phases was also determined by XRD before conducting the TEM experiments and analysis. Additional information about the lattice constants and atomic structure can be gathered from HRTEM (Fig. 28e). We also noticed that the particles do not form one solid structure with an interface (Fig. 28b). The c-BN particle is obviously located on top of the h-BN particle.

* https://next-gen.materialsproject.org/

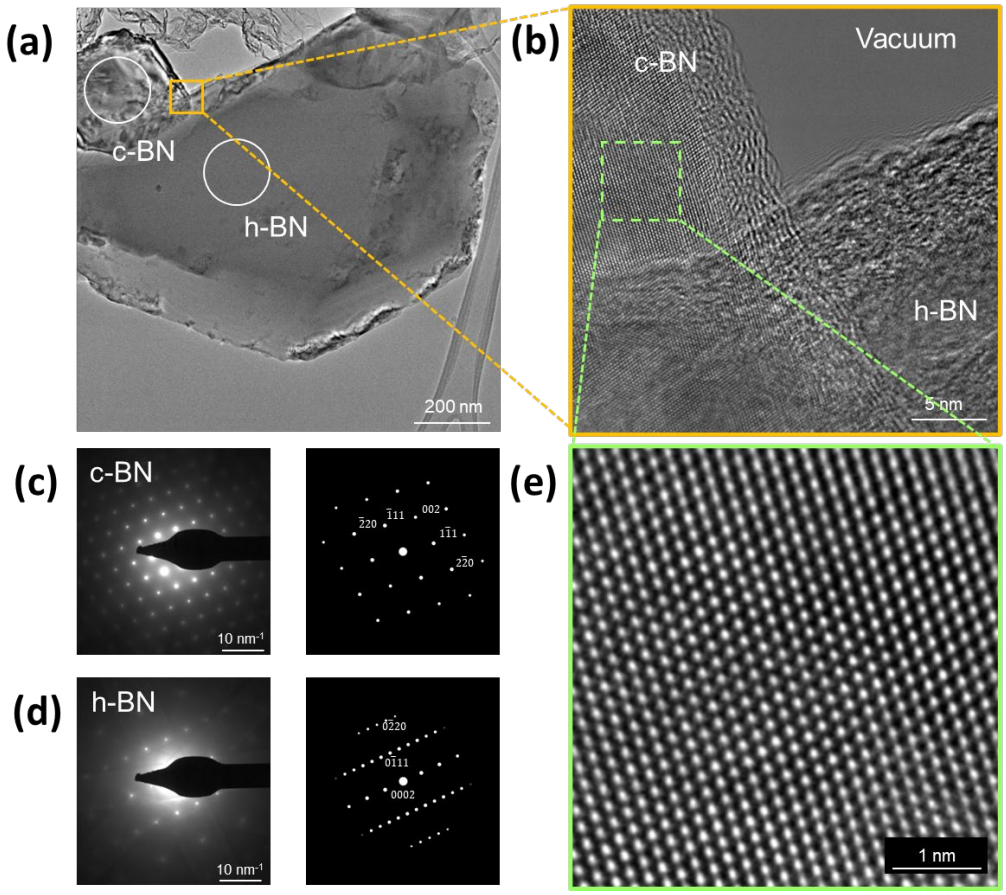

Fig. 28 TEM analysis of the h-BN and c-BN particles. (a) TEM image of two particles with c-BN and h-BN phases. (b) Magnified region with interface of two overlapping particles. (c) SAED and diffraction pattern simulation of the (110) c-BN and (d) $(10\bar{1}0)$ h-BN particles. (e) High-resolution image of the region in b.

These two projects contributed to understanding the c-BN/h-BN phase transition diagram: by investigating the possibility of phase transition in high vacuum conditions and heating the c-BN powder to 1200 °C, and then by analyzing two phases of BN at the turning point of 1500 °C and proving the existence of both c- and h-BN particles after SPS at 90 MPa.

5.3 Diamond/c-BN Interface on N-Functionalized Substrate

The main goal of the collaboration between ARL and Rice University was to epitaxially grow the c-BN on top of the SCD. This task has proven to be very challenging from both the growth and characterization perspectives. The first evidence of successfully growing this interface we acquired by using nitrogen functionalized SCD with 2000 shots of BN deposited by PLD at 500 °C and 100 μTorr (Fig. 29a). HRTEM shows the brighter region on top of the diamond that has the same cubical lattice. This region is not uniform and varies in thickness from

2 to 5 nm along the cross-sectional lamella. Some areas also have a-BN on top of the c-BN as seen in Fig. 29a. The main evidence that this region is c-BN comes from the expanded lattice constant (Fig. 29b) since c-BN has a larger lattice constant compared to diamond. We measured the distances between the (001) planes and displayed them along the multicolored line. Also, since the layer is so thin, the SAED would not give us a proper diffraction pattern, so we had to take fast Fourier transform (FFT) of the bulk SCD and compare them with the mix of SCD and c-BN (Fig. 3c).

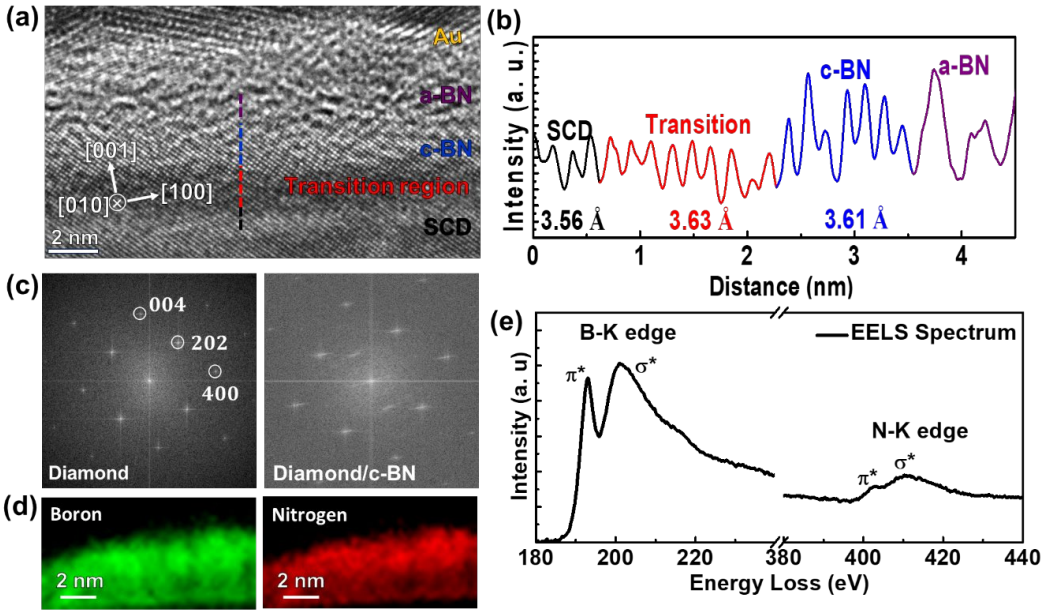

Fig. 29 TEM and EELS analysis of the c-BN/diamond interface. (a) HRTEM image of the c-BN grown on SCD substrate. (b) Plot of the line from (a) denoting the distances between (001) planes for each region. (c) FFT patterns from the bulk diamond and mix of diamond/c-BN areas. (d) EELS maps from the c-BN/diamond interface. (e) EELS spectrum, averaged over the c-BN/diamond area.

As seen from these images, the mix of both materials have additional spots—further evidence of the lattice constants being different. Furthermore, there is a slight mismatch angle (~10°) in the (001) orientation relative to the normal of the sample.

Further investigation was conducted via EELS mapping (Fig. 29d) and spectroscopy (Fig. 29e). EELS resolution is not as good as the EDX mapping; therefore, we must decrease the number of pixels of the map to spend a reasonable amount of time on each map. If we were to increase the number of pixels to get a better resolution image the drift of the sample in the microscope would smear all the interface lines, distorting our data. From the maps that we acquired (Fig. 29d) we can clearly see the existence of both boron and nitrogen in the areas above the diamond. We can also see that these regions start with a more ordered and

structured manner and continue toward rough and disordered, which is how the c-BN and a-BN would look at low resolution on the EELS map. The dark regions above and below the BN maps represent the protective gold layer and the beginning of the SCD, respectively. The spectrum shown on Fig. 29e was averaged over the whole BN region to increase the signal-to-noise ratio (SNR). We can see the signal of the mixed phase of a-/c-BN region. Since c-BN should not have the π* bond it only contributes toward the σ* peak, while a-BN contribution comes to both π* and σ* peaks. This is why we see that the π* peak is lower in intensity than the σ* in both the boron and nitrogen K-edges.

5.4 Influence of HPHT Growth on the BN/SCD Interface

After the first experiment described in Section 1.3 that showed us signs of c-BN/SCD interfaces, several other samples were grown and investigated. One of them includes HPHT diamond substrate that was acid washed with CF6. BN was deposited with PLD at 500 °C, 100 μTorr. Deposition was done in two intervals: 250 shots, break for 10 min, and an additional 2000 shots. Similar TEM analysis was conducted on this sample. The cross-sectional lamella is shown in Fig. 30a. This time, we deposited platinum (Pt) with a Denton Sputter coater before depositing additional protection with FIB. The thickness of BN in this sample varies from the previous (Fig. 30b). The previous sample had around 5 nm of BN with mixed phase; however, the HPHT sample has a varying 12.5–15.5 nm or BN that is amorphous in nature. The atomic resolution image from Fig. 30c shows detailed information about the interface between diamond and a-BN. We see some brighter regions on top of the diamond that is 0.771 nm thick, but we did not see the distinctive change in lattice constant as was noticed before; and the FFT images from such a small region do not produce viable SNR results to compare the spots. This region would require further investigation and analyses. EELS spectrum from the BN region shows amorphous structure since the π* peak is higher in intensity when compared with σ* in the boron K-edge. However, the nitrogen peaks do not show any distinctive peaks, which could mean that either the nitrogen bonding is different or we do not have enough signal to separate them. As said before, this sample would require further experimentation.

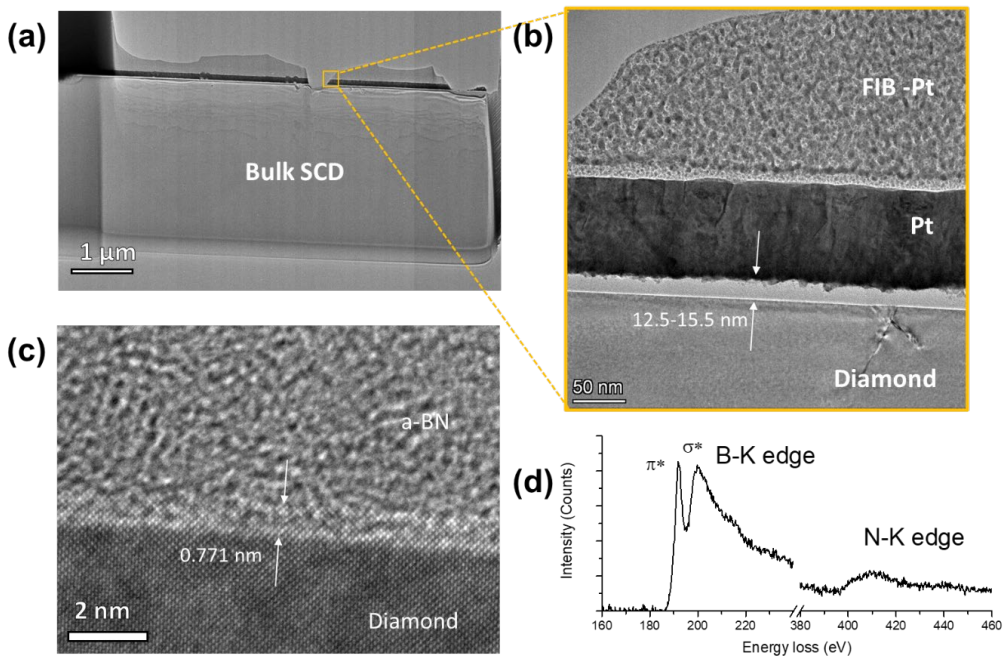

Fig. 30 Investigation of HPHT grown BN on diamond substrate. (a) Overview of cross-sectional lamella for the TEM analysis. (b) Magnified TEM image of the interfaces of the cross section. (c) HRTEM image of the BN/diamond interface. (d) EELS spectrum from the BN area.

5.5 Formation of Graphite Layer via Ion Implantation for Lift-Off Process

Aside from c-BN/SCD interfaces, we were also trying to grow flat diamond surface with a possibility of reusing the substrate for the next epitaxial growth. Thus, we analyzed two samples that were subjected to carbon ion-implantation. The first was a diamond substrate that after implantation had an a-C at an approximately 1.6-µm depth under the surface. The epilayer growth was 1.5 h. The second had an epilayer growth for 2 h and the a-C was turned into graphite.

The cross-sectional lamella overview (Fig. 31a) shows a graphite layer between the diamond layers. Though this is the second/different sample, the structure is the same for both. We determined the structure of the layers using SAED in the 1, 2, and 3 points of the diamond—a-C, graphite, and diamond, respectively. The results of the electron diffraction (Fig. 31b) show the same crystallinity and the regions 1 and 3, while region 2 shows amorphous behavior typical for a-C and graphite. Atomic resolution images of the interfaces from the first sample show the distorted interface of diamond from the direction of incoming ions and more structured and stable interface in the diamond region where the ion implantation stopped (Fig. 31d). The region in between has an amorphous structure.

The key analysis in distinguishing the a-C from graphite was acquired via EELS spectroscopy. Graphite, unlike the a-C, has a σ* bond forming around 293 eV. By comparing the signal from both diamond areas and both a-C and graphite areas (Fig. 31c), we see that the sample with 2-h epitaxial growth has indeed the σ* bond at the corresponding energy value. These spectrums were acquired on UltraSTEM 100 at ORNL and on Titan at Rice University; therefore, we normalized them for the analyses to account for the different counts in EELS detectors.

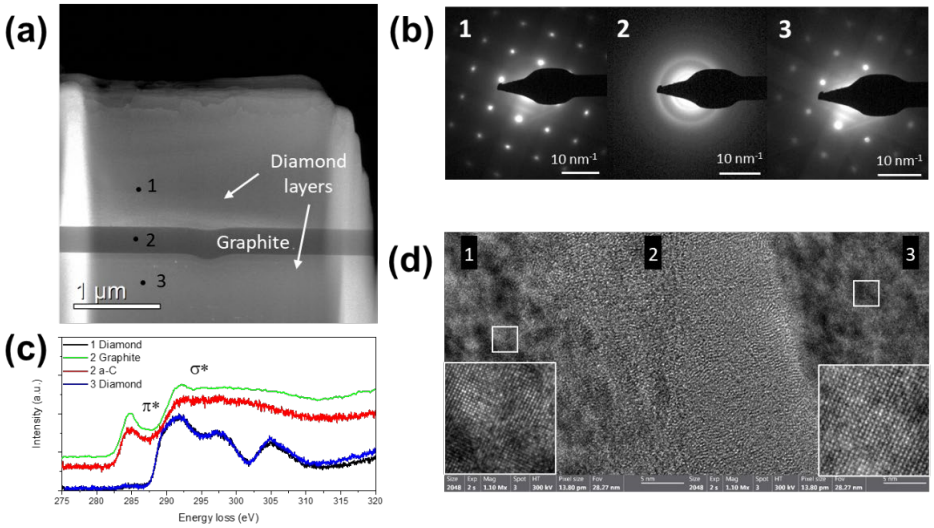

Fig. 31 Comparison of two ion implanted diamond samples with a-C and graphite layers. (a) Overview of the cross-sectional lamella with three regions of interest. (b) SAED taken from 1, 2, and 3 points in (a) showing crystalline diamond in 1, 3 and a-C in 2. (c) EELS spectrum from two samples from the same points in (a). Sample with graphite has additional σ* bond compared with the sample with a-C. (d) HRTEM images from the sample with a-C showing both interfaces: 1-2 and 2-3.

5.6 MPCVD Assisted Growth of BN on Diamond

One of the last experiments conducted in search of the stable c-BN/SCD interface was done on the sample with growth assisted by MPCVD. The sample was prepared for cross section in a similar manner to the previous two, but this time we deposited titanium as a first protective layer to diminish the overexposure of the scanning transmission electron microscopy (STEM) detector during imaging both high Z number gold and low Z number carbon and BN elements.

We can estimate the thickness of the BN layer from the HRTEM image shown in Fig. 32a (12–15 nm at different points around lamella). We can also notice that the BN is not entirely amorphous since there are some crystalline lines present in the middle of it. These lines resemble the turbostratic BN, which is the h-BN-like structure that does not have long-range bonding and cannot form a continuous crystal lattice. This type of behavior is typical along the majority of the interface in

the lamella; however, one region shows a different contrast that looks similar to the sample described in Section 1.3 (Fig. 6c and 6d). STEM imaging shows the same contrast difference, but inverted as would be expected from the dark field imaging. No lattice expansion was found in this region and the FFT, although low in SNR, did not show additional spots for this region. EELS spectrum gathered from this region shows behavior closer to a-BN or h-BN than to c-BN since the π* peak is much higher than the σ* peak in the B K-edge. It is also present in the nitrogen K-edge.

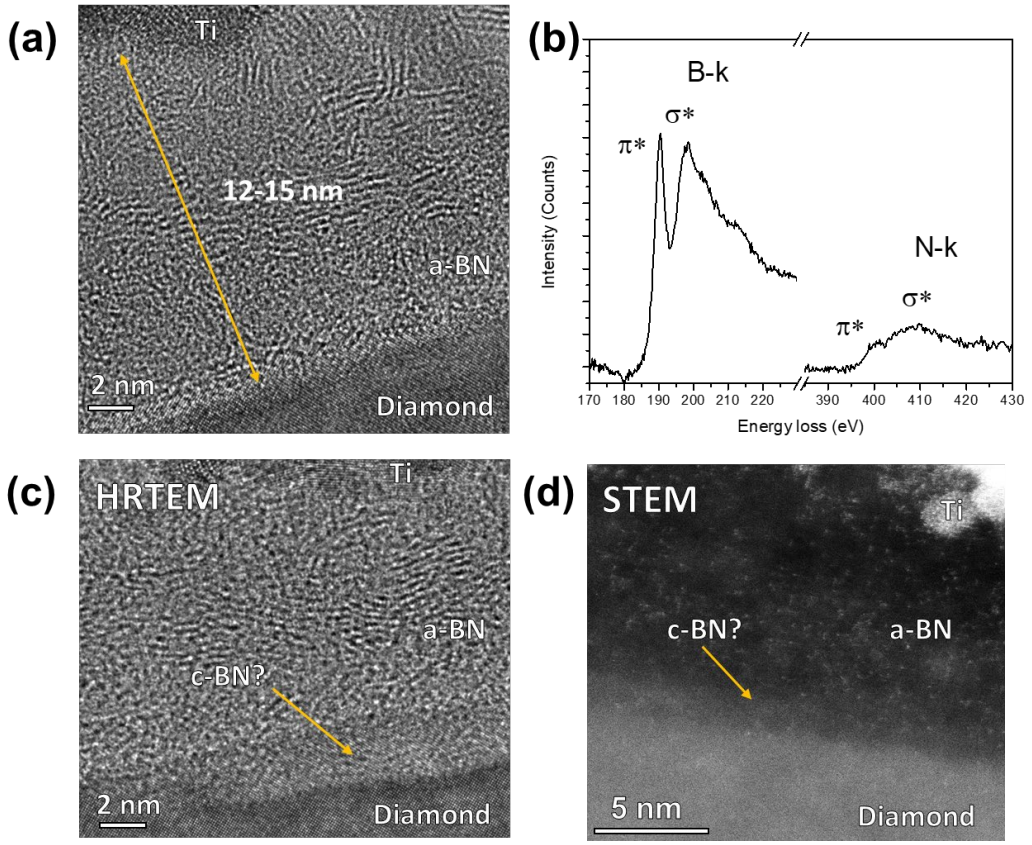

Fig. 32 HRTEM and EELS analysis of the microwave plasma CVD sample. (a,c) HRTEM images of the BN interface showing the interface composition, total thickness of the BN layer, and anomalous step in diamond that has similar features to c-BN. (b) EELS spectrum showing predominantly a-C signal with high π* bond. (d) STEM image with inverse contrast showing that same region in (c) has also reduced contrast in STEM.

6. Terahertz (THz) Spectroscopy: Electrical and Electronic Properties of H-Terminated Diamond

The key advantage of ultra-fast THz spectroscopy lies in its capability to provide the complex-valued THz frequency-resolved conductivity spectrum for the materials under examination. This is achieved through the interaction between the material and ultra-short, sub-picosecond single-cycle pulses of electromagnetic

radiation within the THz frequency range. Notably, THz frequencies align with the typical momentum scattering rates of electrons and holes (carriers) in metals and semiconductors. Additionally, due to the low photon energy (1 THz ≡ 4.1 meV), THz spectroscopy specifically probes the conduction of cold, Fermi-level electrons. This contrasts with laser-excitation methods like two-photon photoemission and second harmonic generation.

Furthermore, THz spectroscopy operates as an all-optical method, and the absence of contacts in measurements, coupled with the (sub-)picosecond interaction timescale, prevents spin accumulation at the contacts. Most importantly, THz spectroscopy exhibits a critical capability to independently determine various carrier transport parameters simultaneously. This is exemplified in cases such as the evaluation of Drude conductivity in metals and semiconductors.

$$\hat{\sigma}(\omega) = \frac{\sigma_{d.c.}}{1-i\omega\tau};\ \sigma_{d.c.} = \frac{e^2\tau N}{m^*} \quad (1)$$

Where $\hat{\sigma}(\omega)$ is the AC conductivity, $\sigma_{d.c.}$ is the DC conductivity, ω/2π is the THz frequency, N is the carrier density, τ is the momentum scattering time, and m^* is the effective mass. We have been actively engaged in implementing optical readout for the electrical properties of transfer-doped diamond wafers through THz time-domain spectroscopy, and our progress has been steady over the past year. The focus of our investigation includes pristine diamond, SCD bulk-doped with boron (doping level 1 × 10^18^{-21} cm^{-3}), H-terminated electronic grade diamond with atmospheric adsorbates as transfer dopant, and another H-terminated electronic-grade diamond wafer with 12-nm Al_2O_3 as transfer dopant. This will help to make a fair comparison between undoped, bulk-doped, and delta-doped samples. The images of the samples used are depicted in Fig. 33.

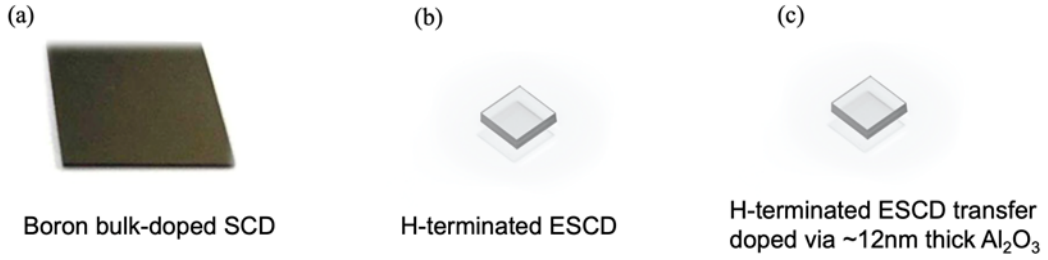

Fig. 33 (a) SCD bulk-doped with boron. (b) Hydrogen terminated electronic-grade diamond wafer and (c) with 12-nm Al_2O_3 as transfer dopant.

The instrumentation employed for THz-TDS measurements is as follows: a laser with a wavelength of 775 nm, a pulse duration of 150 fs, and a repetition rate of 1 kHz is used to pump a nonlinear crystal like $LiNbO_3$ and ZnTe. $LiNbO_3$ generates a broadband pulse in the range of 0.3–1.6 THz, while ZnTe generates pulses within

the range of 0.3–2.5 THz. Detection of THz is accomplished through electro-optic sampling using ZnTe.

Throughout the measurements, we took precautions to maintain a moisture-free atmosphere around the samples to prevent the parasitic absorption of the THz probe beam by moisture. However, isolating the samples from humidity may lead to a reduction in charge carrier density due to the decrease in surface adsorbent molecules, subsequently affecting the DC conductivity for the sample with atmospheric adsorbates as transfer dopants.

The THz intensity profile for air, pristine sample, bulk- and transfer-doped samples, and percentage of absorption for bulk- and transfer-doped samples are provided in Fig. 34. A shift in the THz intensity profile is readily visible between air, pristine, and doped samples. While a 60% absorption is observed for B-doped samples, only 20% or less absorption is observed for transfer-doped samples. This observation is justified in terms of carrier density and their distribution across the thicknesses of the wafer. For, B-doped samples that are bulk-doped, the carriers are distributed across the whole wafer thickness; but, in the transfer-doped sample the carrier distribution is limited to 5–10 nm from the surface. In addition, a 10% field loss was observed in even a pristine sample, implying the net absorption is about 50% for a B-doped sample and below 10% for transfer-doped samples.

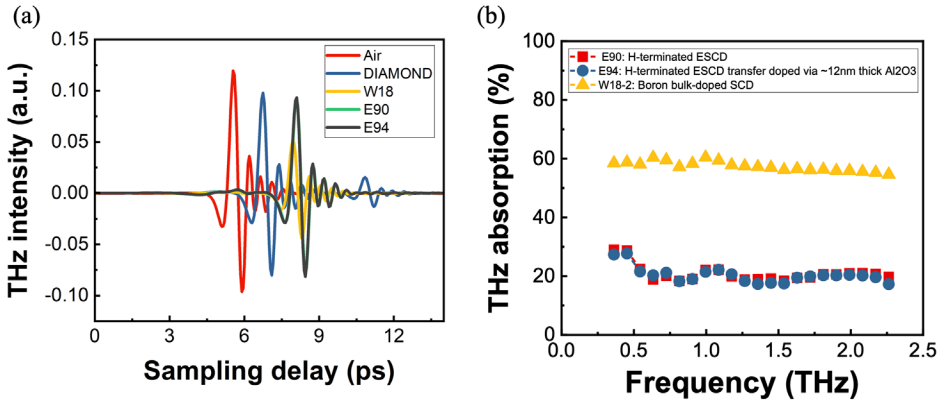

Fig. 34 (a) The THz intensity profile against sampling delays for air, pristine diamond, and bulk- and transfer-doped samples. (b) The percentage of THz absorption observed for bulk- and transfer-doped samples within the 0.2–2.3 THz range.

Later, the optical constants of the B-doped sample and pristine samples were derived—as they are homogenous across the thickness of the wafer—and compared. The variation of the refractive indices and absorption coefficient across 0.4 and 2.4 THz are depicted in Fig. 35. The variation observed in refractive indices is just 0.02 between the pristine and B-doped sample and a variation of 25 cm^{-1} is observed in absorption coefficients. As there are no free carriers in a pristine sample, the absorption of THz pulses is expected to be zero, which is reflected in

the spectrum. Later, the DC conductivity values were deduced per the Drude model and are provided in Fig. 35c. Interestingly, the conductivity values computed via THz match closely with the values derived via DC probe measurements.

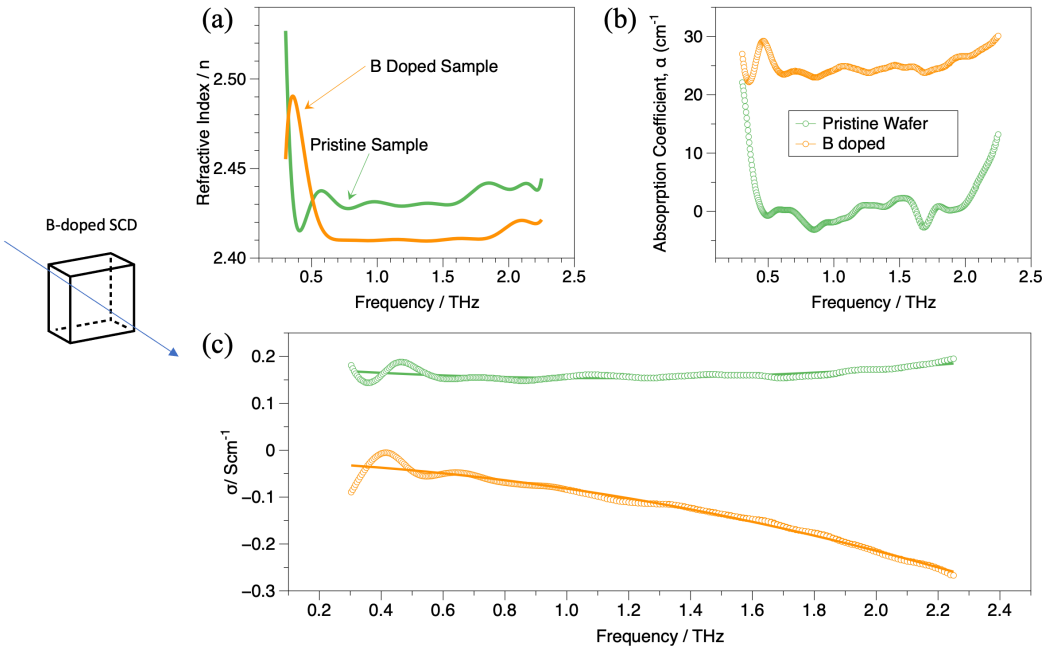

Fig. 35 (a) Refractive indices spectra and (b) absorption coefficient spectra for pristine and boron bulk-doped samples, respectively, at THz frequency. (c) The real (green) and imaginary (orange) conductivity values for B-doped samples.

Since boron bulk-doped diamond has an ionization energy of 0.37 eV, we also measured the photoconductivity in B-doped diamond with an excitation wavelength of 800 nm. Strong photoconductivity is observed from B-doped diamond that follows Drude dispersion. The photoconductivity decay curves and frequency-dependent conductivity values are displayed in Fig. 36. The scattering time of the carriers is approximately 20 fs.

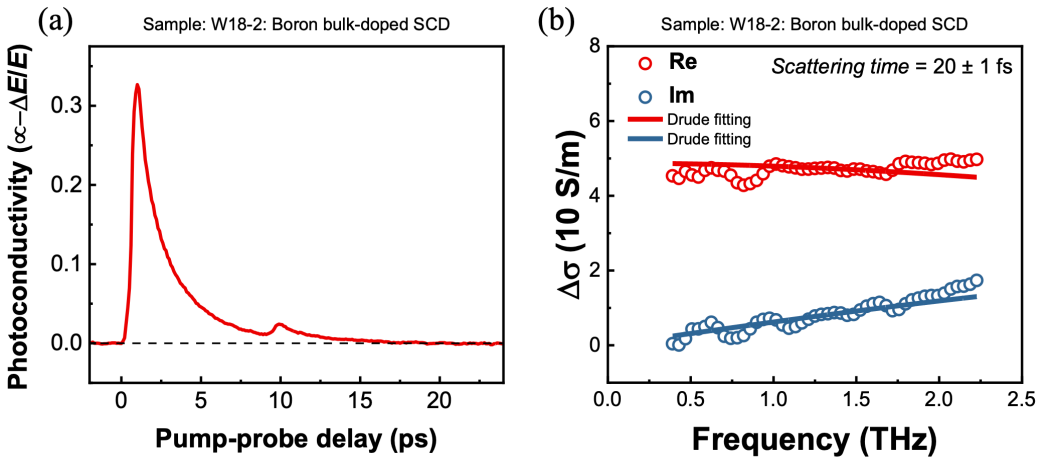

Fig. 36 (a) The photoconductivity decay curve by pump probe experiment and (b) the frequency dependent real and imaginary photoconductivity with Drude fitted curves

Since the transfer-doped samples have different thicknesses and free carrier distribution, a direct derivation of optical constants is not feasible. To deduce the electrical conductivity, THz spectra is processed via thin film model, and then the real and imaginary conductivities' values are obtained (Fig. 37). Although the carrier density is expected to slightly differ for atmospheric dopant and Al_2O_3 dopant, the conductivity values are very similar for both the samples, which matches the values derived from the DC probe measurements.

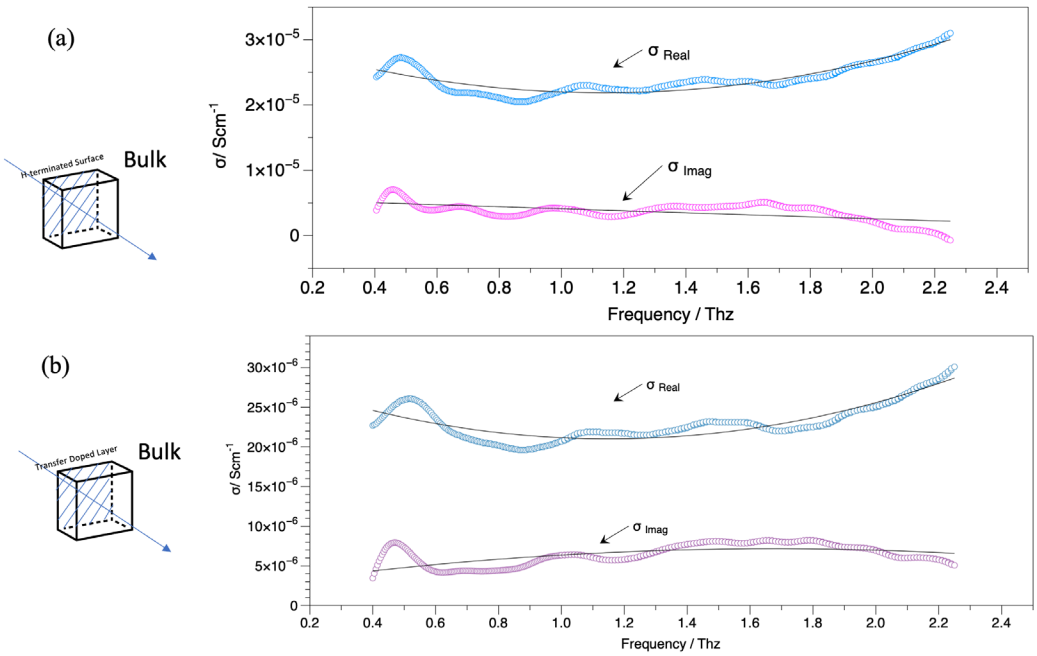

Fig. 37 Schematics showing the sample geometry where the shaded area is the surface that is transfer-doped either via atmospheric adsorbates or by a 12-nm Al_2O_3 layer. The arrows mark the direction of propagation of THz signals, which are depicted on the left-hand side of the figures. (a) The real and imaginary conductivity for H-terminated samples with atmospheric adsorbates as transfer dopants and (b) with 12-nm Al_2O_3 transfer dopants.

7. Diamond Surface Engineering: Inductively Coupled Plasma-Reactive Ion Etching Treatment

Diamond is an exceptional material for electronics due to its remarkable physical and chemical properties. Its high thermal conductivity, wide bandgap, and exceptional hardness make it an ideal candidate for various electronic applications.[14] Diamond-based electronics exhibit superior performance in high-power and high-frequency devices and radiation detection systems. The MPCVD technique is of particular interest for growing diamond, as it allows for precise control over the deposition process, enabling the production of high-quality diamond films essential for advancing electronic technologies.

To grow high-quality homoepitaxial layers of diamond, smooth substrates with low surface defects must be used. These defects, which can either be inherent to the bulk material or the result of polishing-induced damage, are suspected to extend well below the surface of the material, acting as charge traps and scattering centers that can negatively impact the electrical performance of the grown material.[15] To address this, we have explored the use of inductively coupled plasma-reactive ion etching (ICP-RIE) as a pregrowth treatment that could remove layers of the substrate and create a smooth, defect-free surface prior to growth.

The ICP-RIE system uses RF to excite one or more gaseous species into a plasma that etches away at the surface at RT. Unlike traditional RIE, ICP-RIE has two coils that enable separate control of the ion energy and density for more precise etching. Compared to other device materials such as silicon, the influence of the parameters of the ICP-RIE process on diamond is not well understood. Furthermore, only minimal consideration has been given to the quality of growth on the ICP-RIE–treated substrates in literature thus far.[16] Therefore, through this work we have aimed to systematically optimize the conditions of ICP-RIE treatment for the preparation of smooth diamond substrates that can be used for high-quality CVD growth and future device applications.

Our investigation involved a comparative analysis of the etching effects induced by ICP-RIE plasma on polycrystalline diamond substrates with six distinct gaseous species (Fig. 38). The best smoothening effects were observed for SF_6/O_2, yielding a root-mean-square (R_q) roughness as low as 0.613 nm, while $CF_4/Ar/O_2$ plasma resulted in the highest roughness of approximately 1.068 nm. Etch pit concentrations were notably high for Ar/O_2 and $CF_4/Ar/O_2$ treatments, suggesting a physical etching influence exerted by argon gas species.

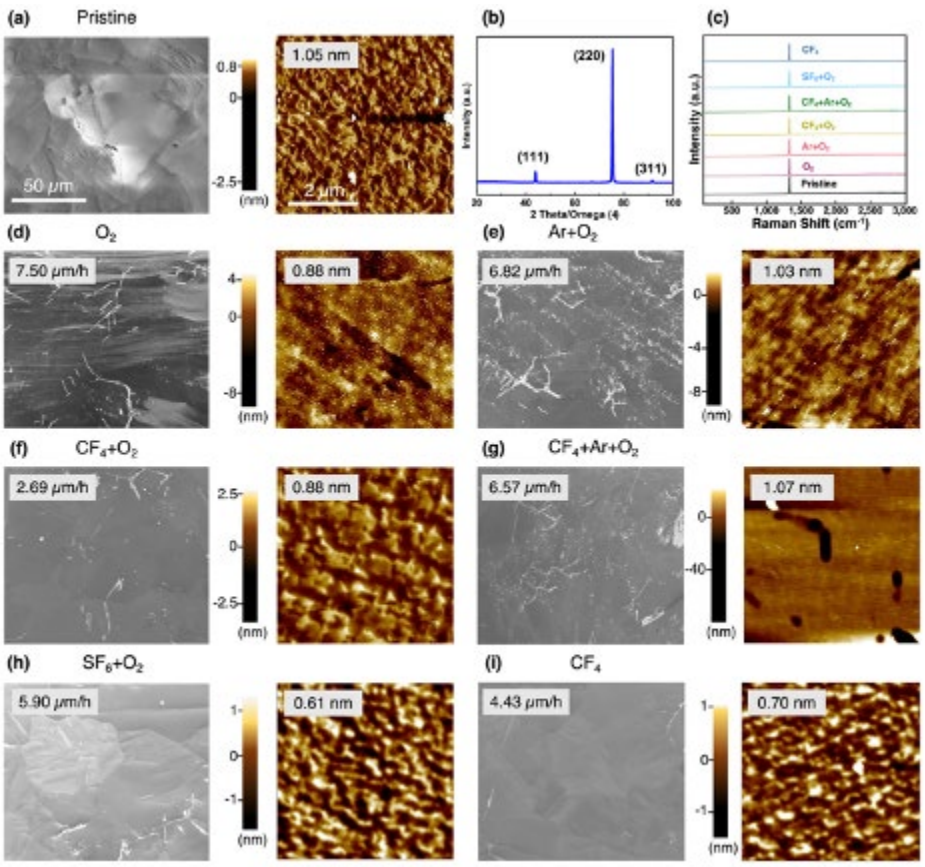

Fig. 38 (a) SEM and AFM images and (b) XRD pattern of pristine polycrystalline diamond (PCD). (c) Raman spectra of pristine and plasma-treated PCD samples. SEM and AFM images of PCD treated by (d) O_2, (e) Ar/O_2, (f) CF_4/O_2, (g) $CF_4/Ar/O_2$, (h) SF_6/O_2, and (i) CF_4 used to analyze roughness and morphology. Roughness obtained from the R_q values.

As shown in Fig. 39, XPS measurements of the samples treated with F-containing species revealed surface fluorination, with the CF_4-treated sample displaying the highest F:C ratio (34.8%); $CF_4/Ar/O_2$ resulted in the lowest ratio (19.3%). High-resolution C1s core level scans indicated dominance of the C–O bond in treated samples, with SF_6/O_2 and CF_4 showing some sp^2 carbon. Furthermore, CF_4/O_2 emerged as a promising subject for further investigation due to its low roughness, minimal etch pits, and absence of graphitization signatures. Exploring the CF_4 to O_2 ratio revealed an ascending trend in surface roughness with increasing CF_4 content. The 20:50 ratio showed minimal etch pits, low surface roughness, and the highest F:C elemental ratio.

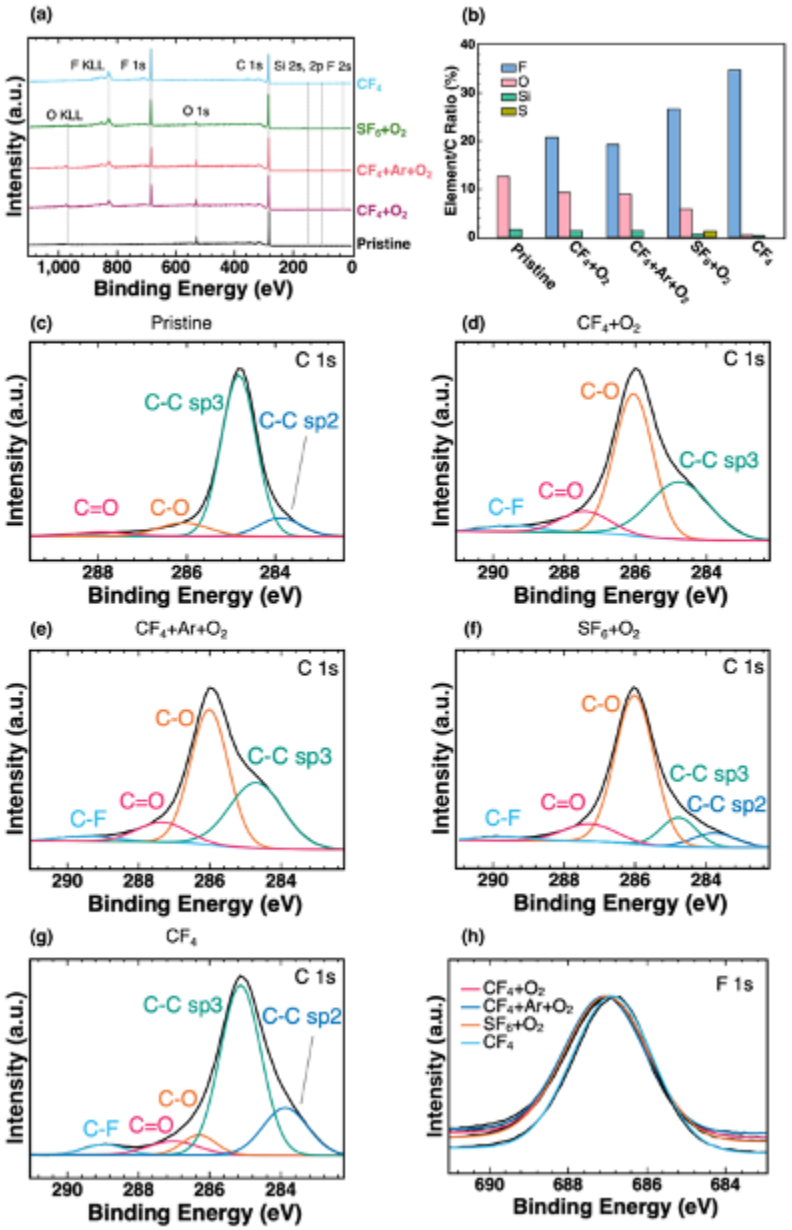

Fig. 39 (a) XPS survey scans of the surfaces treated with F-containing species (CF_4/O_2, $CF_4/Ar/O_2$, SF_6/O_2, and CF_4). (b) Analysis of the ratios of F, O, Si, and S to C on the surfaces. High-resolution C1s core-level scans of (c) pristine PCD and PCD treated by (d) CF/O_2 plasma, (e) $CF_4/Ar/O_2$ plasma, (f) SF_6/O_2 plasma, and (g) CF_4 plasma. (h) High-resolution F1s core-level scans of surfaces treated with CF_4/O_2, $CF_4/Ar/O$, SF_6/O_2, and CF_4.

The influence of coil and bias power on the ICP-RIE process for CF_4/O_2 (20:50) was studied. Coil power significantly affected etch rates, while bias power had minimal impact on either etch rate or surface roughness. Time of flight secondary ion mass spectroscopy (ToF-SIMS) analysis confirmed uniform surface fluorination, with a clear interface between the fluorinated layer and pristine bulk

diamond. Coil power's predominant influence on etch rate suggested that chemical etching dominated the process.

Lastly, contact angle measurements indicated increased hydrophobicity with higher F:C ratios (Fig. 40). The correlation between the F:C ratio and contact angle reaffirmed the hydrophobic nature induced by fluorination. Oxygen termination decreased contact angles, emphasizing the hydrophilic impact. The addition of O_2 and physical etching induced by Ar plasma also influenced the surface's hydrophilic characteristics. The results provide comprehensive insights into the interplay of surface modifications during the ICP-RIE process.

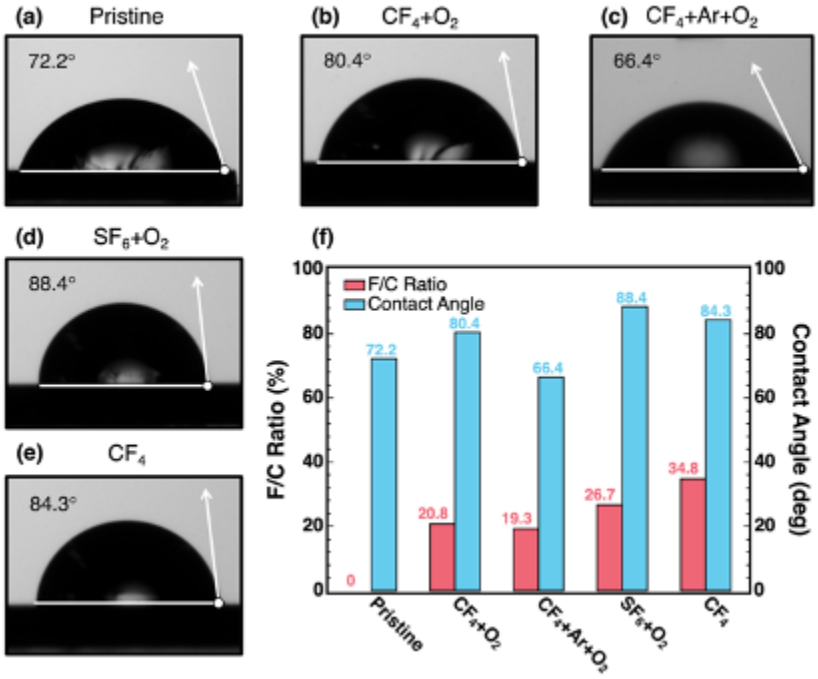

Fig. 40 Contact angle measurements for the surface of (a) pristine PCD, (b–e) PCD samples treated with CF_4/O_2, $CF_4/Ar/O_2$, SF_6/O_2, and CF_4. (f) Respective comparison of F:C ratio (%) and measured contact angle for all the samples.

More recently, we explored the use of Ar + Cl_2 gas for etching SCDs. These, as compared to PCD, are more expensive but preferable for future electronic device applications. We have now started to employ the use of XRD reciprocal space mapping as a means of studying crystal quality both pre- and postetching. Reciprocal Space Mapping (RSM) is a technique that provides a comprehensive view of the crystal lattice structure and its variations. By employing XRD, RSM enables us to study the crystal quality both before and after the etching process. It provides detailed information about crystal orientation, lattice strain, and defects, offering a thorough understanding of the material's structural integrity. Furthermore, after preparing optimally smooth SCD substrates via ICP-RIE, we

investigate using them for the homoepitaxial growth of diamond layers via microwave plasma CVD.

8. Diamond Nanowires via Reactive Ion Etching and Its Electrical Properties

Our fabrication scheme involved standard nanofabrication and lift-off techniques, which are schematically shown in Fig. 41. The PCD (thermal grade, 10- × 10- × 0.3-mm) plate was procured from Elemental Six Inc, and subjected to acid wash (H_2SO_4/HNO_3) before use. The positive photoresist (PR) (PZ 4350) was spin-coated on a PCD substrate with 3500 rpm to form a roughly 10-μm-thick layer followed by postbaking for 1 min under 100 °C. The circular arrays, 5 μm in diameter with 7-μm pitch size and 10 μm in diameter with 12-μm pitch size were designed and generated by KLayout. The exposure time was optimized to 0.64 s for ideal resolution by Maskless photolithography. After the patterns were developed, the forwarding steps involved metallization (Al, Ag, Au, and Au) and stripping (in sonication bath). To ensure full removal of PR during stripping, an e-beam evaporator was chosen as it mostly keeps PR's sidewall unaffected during metal deposition. Then, 200-nm masks were deposited on a diamond plate and optically inspected before RIE. The diamond plates with patterned metal masks on surfaces were etched by inductive coupled plasma with O_2 and Ar gas flow rates of 30 and 90 sccm, respectively. The etching duration varied depending on the experiment. The power supply was set to 1000 W and biased RF power was 200 W. The chamber pressure was 200 mTorr. The etching profiles are shown in Fig. 42a and 42b. The lateral view from SEM indicated that cluster-like diamond nanorods (DNRs) were fabricated with a height of roughly 6 μm and a diameter of roughly 5 μm. The top-view presented that the DNRs have an open end in the central area, meanwhile the ones on the edge tend to be solid. This finding implies the possibility of hollow DNRs fabrication.

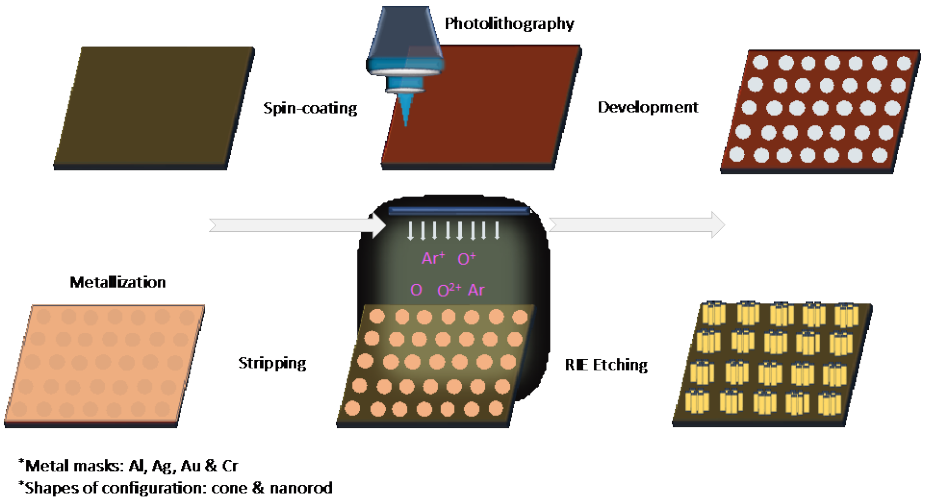

Fig. 41 PCD plate was first acid-washed to remove surface contaminants. Traditional nanofabrication and lift-off techniques were applied to pattern PR and form metal masks on the diamond surface before RIE in Ar/O_2 ambient. The configuration of fabricated DNRs was in either cone or cluster depending on etching mask.

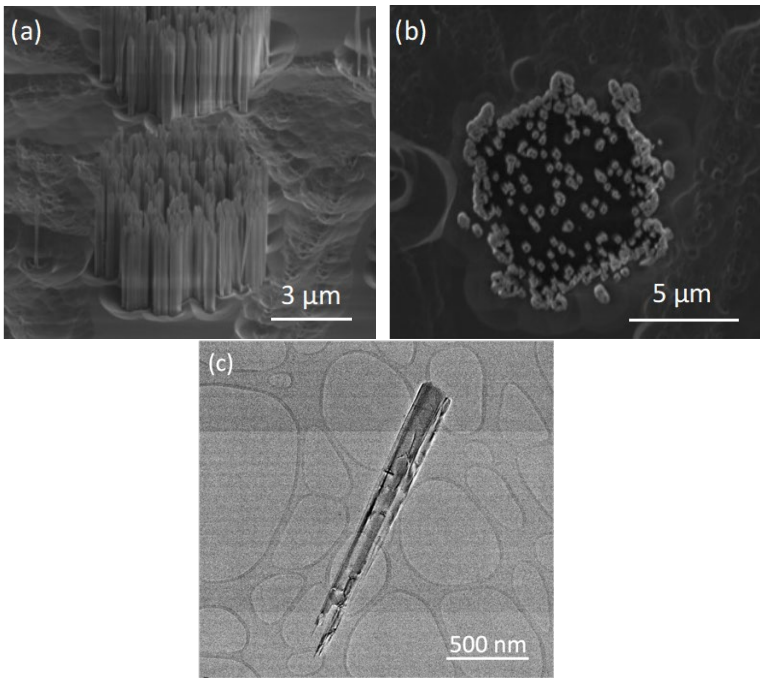

Fig. 42 The lateral (a) and top (b) views of fabricated DNRs showing a cluster-like feature with the ones in the open-ended center. TEM imaging shows the independent profile of DNR.

9. Quantum Emission from Fluorine Vacancies in Diamond

Optics and quantum information processing advancements are largely driven by the incorporation of optically active defects, commonly referred to as "color centers," deliberately embedded in the crystal structure of diamond. One standout among these defects is the negatively charged nitrogen-vacancy (NV^-) center, prized for its attributes such as photo-stability at RT, elevated quantum efficiency, and distinctive spin properties. These qualities make NV^- centers highly promising for applications in quantum sensing and computing.

In the pursuit of single-photon emitters with specific opto-physical characteristics, such as a high emission rate and narrow linewidth, researchers have expanded their exploration beyond the NV complex in diamond. This exploration involves investigating and characterizing alternative optical centers, including group-IV impurities (Si, Ge, Sn, and Pb) and noble gases (He, Xe). The synthesis of color centers in diamond is a crucial aspect, and ion implantation has emerged as a potent technique for precisely engineering a diverse range of color centers. This technique provides control over parameters like ion species, energy, and other crucial factors in the synthesis process.

Despite the progress thus far, the number of emitters with a reproducible fabrication process for a desired spectral range at RT, and with limited or no damage to the parent diamond lattice, remains limited. There is ongoing comprehensive investigation in this field. Consequently, the development of new luminescent defects, such as fluorine-vacancy (FV) centers (Fig. 43), with desirable spectral and quantum emission properties through high-energy implantation of specific ion species, is a crucial strategy for advancing the field. However, this approach leads to undesirable defects and graphitization in the parent diamond lattice.

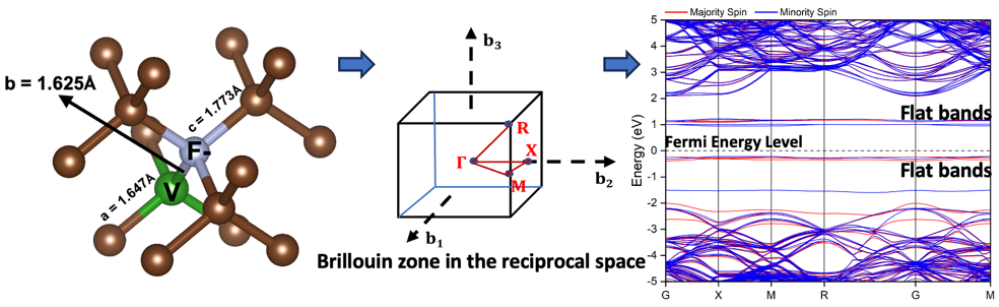

Fig. 43 The local atomic-level structural distortion in cubic diamond with FV center followed by the Brillouin zone in the reciprocal space. Finally, the band diagram, FV is magnetic; there is splitting between spin-up and spin-down bands and the energy gap is reduced and has flat bands near the Fermi energy.

In this context, we have attempted alternative yet viable approaches, including gas-phase fluorine exposure of SCD wafers and low-energy ion-implantation at RT and elevated substrate temperatures. These methods could create FV centers in diamond, serving as an alternative analogue to NV^- centers, with more desirable photoemission properties at RT. The next steps would involve a systematic characterization of photoluminescence (PL) under varying optical excitation energies and temperatures.

9.1 Synthesis of FV Centers in SCD via Gas Phase Fluorination

Although a variety of techniques are available to fluorinate diamond surfaces, here there is a necessity to pursue a morphological and optical defect focused study within the context of an extremely facile approach. We have therefore—based on preliminary experiments performed at the laboratory—as a first step, adopted a simple non-plasma gas phase approach to fluorinate SCD surfaces (Fig. 44). A lab-built Monel reactor is used as the reaction chamber given its nonreactivity and noncorrosive nature when exposed to the harsh fluorine environment. Gas cylinders with a 10% fluorine–helium mixture and helium were separately used as a part of the reaction setup. Helium served as a purging agent to evacuate ambient air in the absence of a vacuum pump. In short, the experimental procedure involved solvent-washing and vacuum-drying the SCD substrate to remove surface adsorbates with acetone and IPA before starting the experiment. At a minimum of 1 h, helium was allowed to purge the chamber prior to the fluorination. The temperature was controlled using a hot plate and strictly increased until thermal equilibrium was achieved, only during the purging stage. The boundary conditions for temperature and time would vary from ambient RT and 30 min to 350 °C and 6 h. Within these condition limits, several experiments are designed, varying time and temperature to study the effect of temperature and time on the fluorination of the diamond surface.

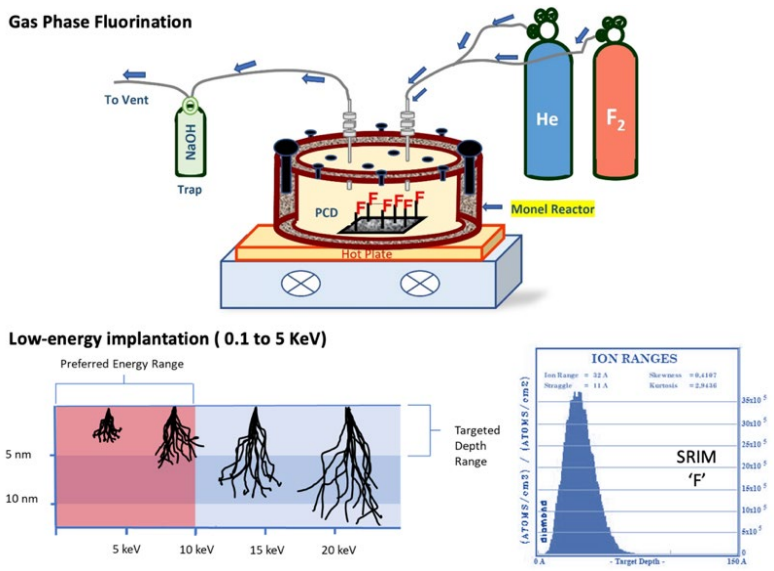

Fig. 44 (Top) Schematic showing the gas-phase fluorination setup, which involves He purging followed by F gas at RT and 350 °C. (Bottom) Schematic showing the proposed low-energy implantation process where the ions can be placed to the very surface region without damaging the parent lattice. The stopping and range of ions in matter (SRIM) projection of the distribution of implanted F ion in the diamond lattice with respect to the depth (right).

9.2 Synthesis of FV Centers in SCD via Low-Energy Ion Implantation

Multiple methods of doping diamond have been developed over the years since the realization of its high potential in electronic devices, with plasma CVD and ion implantation being some of the most prominent methods. But in the case of diamond, the high-energy ions often lead to lattice damage and amorphization in the crystal, consequently causing adverse effects for the optical and semiconductor applications. While some of this damage can be rectified by thermal annealing after doping,[17] it often leads to the formation of graphite, and careful optimization is necessary. Low-energy ion implantation is expected to introduce dopant ions to desired depth levels without damaging the diamond structure and realizing FV centers in diamond with competing optical and electronic properties compared to the widely explored wet chemical approaches and high-energy ion implantation (>30 KeV). The schematic showing the variation in the implantation depth against implantation energy is shown in Fig. 44. Based on the preliminary tests, the proposed parameters for F ion implantation are 1.5-keV energy with 1×10^{15} fluence (cm^{-2}) and $1.0–2.2 \times 10^{11}$ flux (cm^{-2}/S) at substrate temperatures of 450 to 800 °C.

9.3 Preliminary Experiments and Results

We have performed preliminary experiments on hypothesized low-energy implantation as well as gas-phase fluorination experiments and the results are encouraging. In both cases, the fluorination experiments performed at RT showed the signature of formation of FV centers in the proximity of the SCD surfaces. The SIMS and PL studies performed on synthesized FV centers in diamond are provided in Fig. 3. The pumping wavelength used was 480 nm using a monochromatic pulsed laser with approximately 1-um beam size, at 0.5-mW laser power. The range of the PL data was collected from 500 to 950 nm (1.3–2.4 eV) at RT under a vacuum of 10^{-5} mTorr. There is a broad emission observed within the 530–950 nm spectral region (1.3–2.3 eV) centered around approximately 700 nm from the pristine sample, which is attributed to the nominal concentrations of substitutional nitrogen present in the SCD substrate within the range of 5–100 ppb level. Interestingly, while investigating the emission spectra from the low-energy implanted wafer and gas-phase fluorinated sample at RT, new additional features were observed across a high-wavelength region that can possibly be attributed to fluorine defect or vacancy centers (F-V). The single narrow emission lines centered at 780 nm with shoulder peaks from location 1 (Fig. 45a and 45b). This clearly differs from the conventional defect centers such as silicon-vacancy (Si-V) and NV.[18] The FV center regions were scanned for possible single-photon emission and emission color and intensity (Fig. 3c). Although the FV center formation is not uniform across the surface, we observed several emission centers (>100-um area) across the synthesized sample surfaces. The diamond lattice is dense; therefore, the diffusion of ions is expected to be minimal. Furthermore, the surface is very unreactive and the formation of active FV centers, even without any activation process via postannealing, is very surprising. This raises questions about the formation energy of such entities in the diamond lattice, which is not very well understood or explained in the literature. Hence, a combination of computational studies, including both DFT and molecular dynamics (MD) simulations, and systematic experiments with varying F exposure time and substrate temperature in gas-phase fluorination, as well as the implantation energy, fluence, and substrate temperature during low-energy implantation, is warranted to understand the phenomena in a predictive fashion. This will help create a homogeneous FV emission center across the proximity of diamond wafer surfaces. In addition, one needs to explore the possibility of forming different chemical environments of FV centers, like NV centers in diamond, such as FV^0, FV^-, FV^+, and their magnetic ordering and spin states, and spectral emission wavelengths. Such exploration leads to the identification of the tunability of emission wavelength, magnetic sensing behavior,

and the possibility of quantum entangled FV center states, leading to quantum computation-level applications.

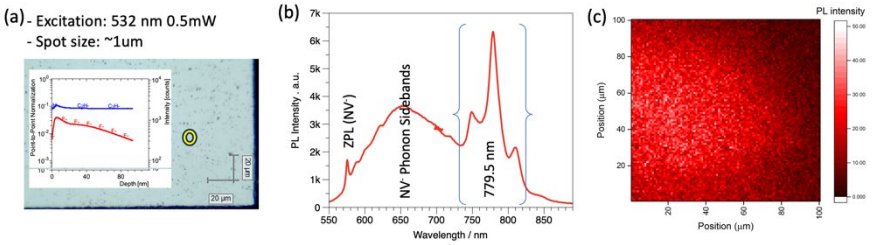

Fig. 45 (a) The single crystal wafer with FV center formed near the surfaces. (b) PL spectra of FV diamond excited with 480 nm. (c) Emission observed from the scanned regions.

10. Conclusions

This report compiles various research activities conducted under the cooperative agreement between Rice University and ARL. These efforts are focused on the collaborative development of diamond as the next-generation UWBG material for electronic devices. The Rice University team brings extensive experience in high-quality materials growth and development, while ARL contributes significant expertise in diamond-based device development. Synergies between the two teams were developed during the first year of the project, leading to the formation of a strong collaborative team.

With support from ARL and substantial investment from Rice University, a state-of-the-art diamond growth facility has been constructed at Rice University and is now operational. Progress during the third year of the program is expected to include the preparation of high-quality samples for use by the ARL team in device fabrication. This includes attempts to grow SCD substrates and heteroepitaxial growth of diamond and c-BN, both considered significant advancements in the field. Significant work has been done in the first 2 years to optimize the growth of high-quality h-BN and transfer them onto H-terminated diamond substrates, with these samples already sent to ARL for device fabrication.

The core of the project is the creation of diamond-based hetero-interfaces, and several such heterostructures have been successfully synthesized and characterized. For BN thin film growth, an advanced-level, load-lock, and ion-beam–assisted PLD growth chamber were installed. The growth parameters for BN thin films were optimized and understood, leading to high crystalline quality films on sapphire and other substrates at HPHT, with further improvements in surface quality through in situ annealing. Similar growth conditions were then applied to grow BN films on GaN substrates, as well as on commercially purchased and home-grown PCD and SCD substrates, with in situ annealing also performed in some cases.

Characterizations revealed the formation of possible nanocrystalline c-BN on SCD substrates, without long-range atomic ordering.

Considering the complex phase diagram of BN and related growth kinetics, future efforts aim to adjust and optimize growth parameters to grow epitaxial c-BN thin films on SCD substrates by PLD. This may involve growing films at a much higher temperature, possibly at 1000 °C, and changing substrate crystalline facets, as different facets have different formation energies. Additionally, in situ or ex situ high-temperature annealing (≥1000 °C) may be necessary to obtain pure phase c-BN. The goal is to grow c-BN films not only along (001)-oriented SCD substrates but also along different facets of SCD (e.g., (111), (113)) with different miscut angles and surface roughness to better understand the interfacial relationship between c-BN and SCD, and the consequent device potentials of c-BN/diamond heterostructures, aiming to make high-mobility FET devices. Strong theoretical effort supports experimental activities including growth, surface modification, and doping in diamond.

Another highlight of the second-, third-, and fourth-year efforts has been the development of specific metrology for diamond-based structures. Techniques such as terahertz spectroscopy, cathodoluminescence imaging, second harmonic generation techniques, scanning probe techniques, and others, have been explored for fast and efficient characterization of diamond surfaces, as well as conventional imaging and spectroscopy methods. Characterization of materials has been synergistic with ARL researchers and facilities. Some device structures fabricated at ARL are being characterized in detail at Rice using FIB slicing and high-resolution TEM, with the FIB milling procedure optimized to prepare TEM specimens of as-grown diamond wafers, diamond-BN hetero interfaces, and diamond-based FET devices, and state-of-the-art microscopy methods employed to characterize these systems with sub-nanometer resolution. The insights gained from these studies will further optimize the device architectures being developed at ARL. Additionally, surface functionalization via wet chemical methods, cleaning the diamond wafer surface via reactive ion etching, and low-energy implantation experiments with low ionization energy alkali metals to create n-type diamond and potential color centers in diamond for quantum emission applications were conducted and optimized.

A strong collaborative team has been established between Rice University and ARL, with interactions including bimonthly discussions via Microsoft Teams, phone calls, specimen exchanges, joint publications (several in the pipeline), and facility sharing at both sites. Interactions in the fourth year have been equally strong, with diamond substrates grown at Rice University to be used by ARL in device fabrication, and ARL sharing several HPHT wafers with Rice University for

the growth of B–N epitaxial thin films. The collaboration is expected to extend to other DoD laboratories (e.g., the US Air Force and Naval Research Laboratories) in the fourth and fifth years. The work done in the third year sets the foundation for a long-term collaboration between Rice and ARL toward developing diamond-based UWBG electronic devices for areas such as high-power and RF electronics. The facility established at Rice for diamond growth will also enable other applications of diamond-based materials, such as quantum sensing and computing. The diamond devices built as part of this effort will also create new opportunities in the network platforms being developed as part of the same cooperative agreement.

11. References

1. Neudeck PG, Okojie RS, Chen LY. High-temperature electronics - a role for wide bandgap semiconductors? Proc IEEE. 2002;90(6):1065–1076.
2. Takahashi K, Yoshikawa A, Sandhu A, editors. Wide bandgap semiconductors: fundamental properties and modern photonic and electronic devices. Springer, Berlin, Heidelberg; 2007. p. 1–460.
3. Davis RF, Sitar Z, Williams BE, Kong HS, Kim HJ, Palmour JW, et al. Critical evaluation of the status of the areas for future research regarding the wide band gap semiconductors diamond, gallium nitride and silicon carbide. Mater Sci Eng B. 1988 Aug;1(1):77–104.
4. Chow TP, Tyagi R. Wide bandgap compound semiconductors for superior high-voltage unipolar power devices. IEEE Trans Electron Dev. 1994;41(8):1481–1483.
5. May PW. The new diamond age? Science. 2008;319(5869):1490–1491.
6. Pau M BW. Diamond thin films: a 21st-century material. Trans R Soc Lond A. 2000;358:473–495.
7. Saslow W, Bergstresser TK, Cohen ML. Band structure and optical properties of diamond. Phys Rev Lett. 1966;21(10):715. doi: 10.1103/PhysRevLett.21.715.
8. Wei L, Kuo PK, Thomas RL, Anthony TR, Banholzer WF. Thermal conductivity of isotopically modified single crystal diamond. Phys Rev Lett. 1993;70:3764–3767. doi: 10.1103/PhysRevLett.70.3764.
9. Suzuki K, Sawabe A, Yasuda H, Inuzuka T. Growth of diamond thin films by DC plasma chemical vapor deposition. Appl Phys Lett. 1987;50(12):728–729.
10. Mokuno Y, Chayahara A, Yamada H. Synthesis of large single crystal diamond plates by high rate homoepitaxial growth using microwave plasma CVD and lift-off process. Diam Relat Mater. 2008;17(4–5):415–418.
11. Strobel P, Riedel M, Ristein J, Ley L. Surface transfer doping of diamond. Nature. 2004;430(6998):439–441.
12. Ajayan PM, Vajtai R, Zhang X, Puthirath AB, Biswas A, Oliviera E, Li C, Kannan H, Gray T, Elkins J, Ivanov T, Birdwell AG, et al. Development of diamond-based materials systems for high-power RF electronics: third-year report. DEVCOM Army Research Laboratory (US); 2023 May. Report No.: ARL-TR-9696.

13. Pallas A, Larsson K. Initial growth of BN on diamond substrates: a theoretical approach. J. Phys. Chem. C 2010; 114(26):11448–11455.

14. Arnault JC, Saada S, Ralchenko V. Chemical vapor deposition single-crystal diamond: a review. Phys Status Solidi Rapid Res Lett. 2022;16(1):2100354.

15. Hicks ML, Pakpour-Tabrizi AC, Jackman RB. Polishing, preparation and patterning of diamond for device applications. Diam Relat Mater. 2019 Aug 1;97:107424.

16. Muchnikov AB, Vikharev AL, Butler JE, Chernov VV, Isaev VA, Bogdanov SA, Okhapkin A, Yunin P, Drozdov Y. Homoepitaxial growth of CVD diamond after ICP pretreatment. Phys Status Solidi A. 2015;212(11):2572–2577.

17. Seki Y, Kurashima R, Yoshihara M, Hoshino Y. Optimization of activation annealing condition for boron-implanted diamond. Phys Status Solidi A. 2023;220(19):2300522.

18. Zhang JL, Ishiwata H, Babinec TM, Radulaski M, Müller K, Lagoudakis KG, Dory C, Dahl J, Edgington R, Soulière V, et al. Hybrid group IV nanophotonic structures incorporating diamond silicon-vacancy color centers. Nano Lett. 2016 Jan 13;16(1):212–217.

12. List of Publications

1. Biswas A, Alvarez GA, Tripathi M, Lee J, Pieshkov TS, Li C, Gao B, Puthirath AB, Zhang X, Gray T, Ajayan P, et al. Cubic and hexagonal boron nitride phases and phase boundaries. Manuscript under revision.

2. Xu M, Biswas A, Li T, He Z, Luo S, Mei Z, Zhou J, Puthirath AB, Vajtai R, Ajayan P, et al. Vertical β-Ga2O3 metal-insulator-semiconductor diodes with an ultrathin boron nitride interlayer. Appl Phys Lett. 2023;123:232107.

3. Biswas A, Xu R, Alvarez GA, Zhang J, Christiansen-Salameh J, Puthirath AB, Burns K, Hachtel JA, Li T, Iyengar SA, et al. Non-linear optics at twist interfaces in h-BN/SiC heterostructures. Adv Mater. 2023;35:2304624.

4. Biswas A, Alvarez GA, Li T, Christiansen-Salameh J, Jeong E, Puthirath AB, Li C, Gray T, Kannan H, Zhang X, et al. Structural, optical, and thermal properties of BN thin films grown on diamond via pulsed laser deposition Phys Rev Mater. 2023;7:094602.

5. Biswas A, Xu R, Christiansen-Salameh J, Jeong E, Alvarez GA, Li C, Puthirath AB, Gao B, Garg A, Gray T, et al. Phase stability of hexagonal/cubic boron nitride nanocomposites. Nano Lett. 2023;23(15):6927–6936.

6. Alvarez GA, Christiansen-Salameh J, Biswas A, Puthirath AB, Jeong E, Kwon J, Lee J, Gray T, Vajtai R, Ajayan PM, et al. Cross-plane thermal conductivity of h-BN thin films grown by pulsed laser deposition. Appl Phys Lett. 2023;122:232101.

7. Biswas A, Maiti R, Lee F, Chen CY, Li T, Puthirath AB, Iyengar SA, Li C, Zhang X, Kannan H, et al. Unravelling the room temperature growth of two-dimensional h-BN nanosheets for multifunctional applications. Nanoscale Horiz. 2023;8:641–651.

8. Biswas A, Ruan Q, Lee F, Li C, Iyenger SA, Puthirath AB, Zhang X, Kannan H, Gray T, Birdwell AG, et al. Unidirectional domain growth of hexagonal boron nitride thin films. Appl Mater Today. 2023;30:101734.

9. Biswas A, Xu M, Fu K, Zhou J, Xu R, Puthirath AB, Hachtel JA, Li C, Ajay Iyengar S, Kannan H, et al. Properties and device performance of BN thin films grown on GaN by pulsed laser deposition. Appl Phys Lett. 2022;121:092105.

List of Symbols, Abbreviations, and Acronyms

2/3D	two-/three-dimensional
a-C	amorphous carbon
AC	alternating current
AFM	atomic force microcopy
Al_2O_3	alumina/sapphire
Ar	argon
ARL	Army Research Laboratory
ARO	Army Research Office
B	boron
BCN	boron carbon nitride
BFOM	Baliga figure of merit
BN	boron nitride
C	carbon
CA	cooperative agreement
c-BN	cubic boron nitride
CVD	chemical vapor deposition
DC	direct current
DEVCOM	US Army Combat Capabilities Development Command
DFT	density functional theory
DNR	diamond nanorod
DoD	Department of Defense
EDS	energy dispersive spectroscopy
EDX	electron dispersive X-ray spectroscopy
EELS	electron energy loss spectroscopy
F	fluorine
FESEM	field emission scanning electron microscopy
FET	field-effect transistor
FFT	fast Fourier transform
FIB	focused ion beam
FTIR	Fourier transform infrared
FWHM	full width at half maximum

FV	fluorine vacancy
GaN	gallium nitride
GIXRD	grazing angle X-ray diffraction
H/H_2	hydrogen
h-BN	hexagonal BN
HPHT	high-pressure, high-temperature
HRTEM	high-resolution TEM
ICP-RIE	inductively coupled plasma–reactive ion etching
IPA	isopropyl alcohol
LO	longitudinal optical
MBE	molecular beam epitaxy
MD	molecular dynamics
Mg	magnesium
MPCVD	microwave-plasma chemical vapor deposition
N	nitrogen
NEA	negative electron affinity
NV^-	nitrogen vacancy
O	oxygen
ORNL	Oak Ridge National Laboratory
P	phosphorus
PCD	polycrystalline diamond
PID	pulsed interval deposition
PL	photoluminescence
PLD	pulsed laser deposition
PR	photoresist
Pt	platinum
RF	radio frequency
RHEED	reflection high-energy electron diffraction
RSM	Reciprocal Space Mapping
RT	room temperature
SAED	selected area electron diffraction
Si	silicon
SiC	silicon carbide

Si-V	silicon-vacancy
SCD	single-crystal diamond
SEM	scanning electron microscopy
SHG	Second Harmonic Generation
SIMS	secondary ion mass spectrometry
SNR	signal-to-noise ratio
SPS	spark plasma sintering
SRIM	stopping and range of ions in matter
STEM	scanning transmission electron microscopy
TEM	transmission electron microscopy
THz	terahertz
TO	transverse optical
ToF	time of flight
UV	ultraviolet
UWBG	ultra-wide bandgap
VBM	Valence Band Maximum
XPS	X-ray photoelectron spectroscopy
XRD	X-ray diffraction

1 (PDF)	DEFENSE TECHNICAL INFORMATION CTR DTIC OCA
1 (PDF)	DEVCOM ARL FCDD RLB CI TECH LIB